CONFIDENTIAL

Aerodynamic Design Optimization of the MTT Radial Micro Turbine

S.Govindarajan

Master of Science Thesis

TU Delft Delft University of Technology

Aerospace

MSCCONFIDENTIAL

Aerodynamic Design Optimization of the MTT Radial Micro Turbine

Master of Science Thesis

For the degree of Master of Science in Aerospace Engineering at Delft University of Technology

S.Govindarajan

September 29, 2015

Faculty of Aerospace Engineering(LR)
Delft University of Technology
Thesis Registration Number 052#15#MT#FPP

Delft University of Technology
Department of
Flight Performance and Propulsion

The undersigned hereby certify that they have read and recommend to the Faculty of Aerospace Engineering(LR) for acceptance a thesis entitled

Aerodynamic Design Optimization of the MTT Radial Micro Turbine

by

S.Govindarajan

in partial fulfillment of the requirements for the degree of

Master of Science Aerospace Engineering

Dated: September 29, 2015

Supervisor(s):

Prof. dr. ir. P. Colonna

Dr. ir. M. Pini

Dr. ir. W.P.J. Visser

Reader(s):

Dr. ir. R. Pecnik

Summary

Micro turbines are touted to become the prime system for the combined heat and power(CHP) applications in light of their significant advantages in terms of performance, size, costs and reduced CO_2 emissions [1]. Micro Turbine Technology B.V. (MTT) is currently developing a 3 KW recuperated micro turbine for such applications. Commercially available off the shelf turbocharger components are used since they provide high performance with relatively low costs since they are mass produced.The drawback in using these components is that they are manufactured for the automotive sector and inherently operate at different conditions than the MTT operating point. Here in lies an interesting scope for performance improvement by optimizing the turbine and within the current work the focus is on aerodynamic optimization of the radial inflow turbine used in the MTT system.

This study is a follow-up from the recommendations provided in [2] and [3]. A goal driven optimization is performed on the rotor geometry using ANSYS DesignXplorer and a total of four design solutions were obtained. The most important findings from the response surfaces, sensitivity analysis from the optimization were:

- From the parametric sensitivity it was clear that all of the six design variables have a significant impact on efficiency. The exducer angles have the most predominant effect on efficiency with that of β_{shroud} larger than β_{hub}.
- All of the optimal candidates exhibited an increase in the total-to-total efficiency ranging from a minimum of 6.38 percentage points to a maximum of 7.90 percentage points as compared to the baseline geometry. This efficiency improvement was accompanied by an increase in mass flow rate with a minimum value of 69.15 g/s and a maximum of 73.51 g/s.

These design solutions are then coupled with the diffuser domain to study the performance characteristics and the interaction between the components. The most important outcomes from these simulations were:

- The efficiency of the rotor drops by 3 percentage points on an average due to the additional pressure losses introduced when coupled with the diffuser.
- The diffuser performance has improved and the C_p experiences a maximum increase of 17.63 percentage points (Candidate D) and a minimum of 12.70 percentage points (Candidate B). The swirl coefficient for optimum diffuser performance is found at values close to 0.22. If the swirl coefficient is increased or decreased from this optimum, diffuser performance drops. The best design solution in terms of rotor efficiency and overall total-to-static efficiency is Candidate C. However it exhibits a poorer diffuser performance than the other optimal candidates. From this study, it is apparent that there is compromise between rotor and diffuser performance.
- The improvement in rotor efficiency($\eta_{tt,5_{ax}}$) ranges from a minimum of 6.16 (Candidate A) percentage points to a maximum of 8.54 percentage points (Candidate C) as compared to the baseline which is more or less similar to the case with the individual rotor domain simulations. The improvement in total-to-static efficiency ($\eta_{ts,9}$) achieves only a maximum of 3.23 percentage points(Candidate C) as compared to the baseline. In other words ,whatever is gained in rotor total-to-total efficiency from the design optimization, less than half of it is utilized when coupled with the diffuser(C_p<50 %).

The best candidate solution selected from the simulations mentioned above is then analyzed from a structural point of view by comparing its equivalent von-Mises stresses with that of the baseline design. The most important conclusions from this study were:

- The optimized rotor experiences higher at stresses at the tip station than the baseline. At the root section both geometries exhibit higher stresses than most of the other stations. At the trailing edge the optimized rotor exhibits lower stresses than the baseline geometry. A maximum stress of 1599.7 MPa for the baseline occur at the trailing edge root section and the optimized rotor experiences a lower maximum of 1439.3 MPa and it occurs closer to the shaft.
- In order to reduce the tip stresses for the optimized rotor and bring them closer to the baseline values, the speed of rotation must be reduced to the neighborhood of 180 000 rpm.

One of the important outcomes of this study is that there is a compromise between diffuser and rotor performance, consequently a coupled optimization is recommended with the diffuser domain in order to get a better understanding of the interaction effects between the components. The optimization procedure in this work is performed with only the rotor domain due to computational restrictions and the design solution does not take into account the diffuser performance during the optimization process. A scaling study with the volute is recommended for the optimized rotor geometry in order to restrict the mass flow rate. The design solution exhibits an increase in passage area and consequently a rise in mass flow rate. However, in the real application a change in mass flow rate might cause a mismatch with other components of the MTT power unit. The structural analysis is done post optimization and is carried out without any constraints for maintaining the stress within acceptable levels. Therefore a multi-disciplinary optimization combining the solid and fluid analysis is recommended to prevent the stress increase and maintain the creep life of the component.

Table of Contents

List of Figures

List of Tables

Nomenclature

Latin Symbols

a	Equation coefficient	$[-]$
b_{le}	Tip width	$[mm]$
C	Absolute flow velocity	$[m/s]$
C_s	Spouting velocity	$[m/s]$
c_p	Specific heat	$[kJ/kg]$
C_p	Static pressure recovery coefficient	$[-]$
E	Energy	$[J/kg]$
F	Force	$[N]$
h	Enthalpy	$[kJ/kg]$
I	Stress Invariant	$[-]$
k	Turbulent kinetic energy	$[J/kg]$
m	Mass	$[kg]$
$\dot{m}$	Mass flow rate	$[kg/s]$
N	Rotational speed	$[rpm]$
N_θ	Rotor exit swirl coefficient	$[-]$
P	Power	$[W]$
P_L	Relative pressure loss	$[-]$
p	Pressure	$[Pa]$
R	Radius	$[m]$
s_{ij}	Stress components	$[N/m^2]$
T	Temperature	$[K]$
U	Blade velocity	$[m/s]$
W	Relative flow velocity	$[m/s]$
Z_{axial}	Axial length	$[mm]$

Greek Symbols

α	Equation coefficient	$[-]$
β	Exducer angle	$[degree]$
γ	Specific heat ratio	$[-]$
η	Efficiency	$[-]$
ξ	Total pressure loss coefficient	$[-]$
σ_v	Equivalent tensile stress	$[N/m^2]$
σ^{dev}	Stress deviator tensor	$[N/m^2]$
ϵ	Turbulent dissipation energy	$[J/kg]$
ω	Angular velocity	$[rad/s]$

Subscripts

θ	Circumferential
04	Turbine inlet identifier total-to-total properties
05	Turbine outlet identifier total-to-total properties
4	Turbine inlet identifier total-to-static properties
5	Turbine outlet identifier total-to-static properties
5_{ax}	Turbine outlet identifier total-to- total properties excluding swirl component
9	Diffuser exit properties
atm	Atmospheric
c	Corrected property
hub	Hub station identifier
is	Isentropic
le	Leading edge station identifier
opt	Optimum
shroud	Shroud station identifier
stp	Standard
t	Turbine
te	Trailing edge station identifier
ts	Total-to-static
tt	Total-to-total

Abbreviations

0-D	Zero Dimensional Model
1-D	One Dimensional Model
3-D	Three Dimensional Model
CCD	Central Composite Design
CFD	Computational Fluid Dynamics
CHP	Combined Heat and Power
DNS	Direct Numerical Simulation
DES	Detached Eddy Simulation
GDO	Goal Driven Optimization
LES	Large Eddie Simulation
LES	Large Eddie Simulation
MTT	Micro Turbine Technology
MOGA	Multi-Objective Genetic Algorithm
NLPQL	Non-Linear Programming by Quadratic Lagrangian
NPR	Non-Parametric Regression
OEM	Original Equipment Manufacturer
OSFD	Optimal Space Filling Design
RANS	Reynolds Averaged Navier Stokes
SST	Shear Stress Transport
TIT	Turbine Inlet Temperature

Acknowledgements

I would like to express my sincere gratitude to my supervisors Prof. Dr. Ir. P. Colonna, Dr. Ir. M. Pini and Dr. Ir. W.P.J. Visser for their support, guidance and understanding which added considerably to my graduate experience. Without their valuable assistance and expertise, this work would not have been completed. I would also like to thank Dr. Ir. R. Pecnik for being part of my thesis committee. I would like to thank my friends for their patience and support and most importantly, I would like to thank my parents for their unconditional support throughout my master program.

Delft, University of Technology S.Govindarajan
September 29, 2015

Chapter 1

Introduction

The current chapter will present an overview of the research on micro turbines. The first section presents the motivation behind the work on micro gas turbine followed by its concept and development. The next section will involve a description of the previous research in this field.

1.1 Motivation

With the current advances in electronics and the advent of the age of distributed power systems, the small-scale power generation systems have seen an upward trend in the decentralizing energy sector. The CHP systems which come on-site power generation with the use of by-product heating are becoming increasingly popular and micro turbines are touted to become widespread in this market. Micro turbines are an interesting candidate for such systems as they provide advantages in terms of performance, size and costs [4]. Micro turbines typically range from hand-held units producing less than a kilowatt to commercial systems producing tens or hundreds of kilowatts [5]. With the ever increasing inclination of the prices for conventional fossil fuels, micro turbines provide a more efficient alternative as most of the exhaust heat is recovered and is also put to use. One of the prime technological challenges with the larger gas turbines was the maximum turbine inlet temperature. This paved the way for micro turbines applications with maximizing recuperator performance and also as compared to conventional gas turbines, the micro gas turbines have lesser losses in transmission and distribution due to their size. Hence these CHP concepts for small-scale distributed power generation offer significant potential for saving energy and reducing CO_2 emissions and are typically used to replace heating boilers for households and small businesses [6]. For such CHP applications with typically small scale power generation of up to 100 KW, the radial turbines with their advantages in terms of stress, fatigue and costs are are being preferred now days. The field of micro generation being relatively novel, there is a great opportunity

for research and development of new concepts especially for CHP applications.

Micro Turbine Technology B.V. (MTT) has designed a 3 KW micro turbine for such applications. Development of a micro turbine optimized for a particular cycle is very expensive and one of the prospective methods to overcome this is to make use of the commercially available off-the-shelf turbochargers utilized for automotive applications. Since these are mass produced and provide high performance, they are a cost efficient solution. The major problems when using them for CHP applications is the high rotational speed, turbine inlet temperature, and the efficiency of the components of the micro turbine system [7] [8]. Additionally, these turbochargers operate at a different operating point than the MTT cycle and thus incur further losses. As a result, this puts emphasis on the optimization of the radial turbine design to improve its performance.

1.2 Previous work

This work is a follow up of the work presented by Sol [2] and Gideonse [3]. Sol [2] focused on scroll and exducer blade angle modifications to improve turbine efficiency. Gideonse [3] improved upon these existing 0-D models and developed a CFD model for parametric optimization of the turbine. The conclusions and recommendations from these studies will be discussed in further detail in the following section.

1.2.1 Sol

Scroll and rotor inlet

With the earlier work it was known that the difference in operating point between the MHI and MTT led to a change in absolute velocities and hence resulting in incidence losses. They are due to the difference between the real inflow angle and the optimum inflow angle. Several studies were conducted for scaling the volute characterised by the tongue area to minimize the incidence losses. The 0-D model predicted an improvement in efficiency with increase in tongue area. But the CFD analysis revealed that increasing the tongue area to reduce the incidence losses lead to an increase in corrected mass flow which was counter-productive and ultimately resulted in a drop in efficiency.

Exducer blade angle

This study was conducted to reduce the swirl losses using two evaluation methods. The zero-swirl method assumed all swirl energy as lost and the 10-swirl method assumes a swirl angle of 10° for optimum diffuser performance. Decreasing the current blade angle from 63.70° resulted in an improvement in turbine and diffuser performance. The optimum was found to be around 55° for both the zero-swirl and 10-swirl evaluation methods while taking into account both turbine and diffuser performance.

1.2.2 Gideonse

Scroll and exducer blade angle

The 0-D model was improved with a more accurate loss model and used as a starting point for parametric optimization. It was established by Sol [2] that the mass flow variation occurred while changing the tongue area or the exducer angle separately and would result in decreased efficiency. Hence the volute tongue area was scaled accordingly to maintain the mass flow and this variation was analysed using 3-D CFD models.

Tip diameter

This study was conducted primarily to find the tip diameter that corresponded to the optimal velocity ratio. An increase in the tip diameter from 35 mm to 39.375 mm resulted in an increase in turbine total-to-static efficiency (without diffuser) by 1.4 percentage points but this led to an increase in mass flow by 3.2 %. One of the drawbacks is that the structural issues of increasing the tip diameter were not considered.

Diffuser

The diffuser is primarily used to recover dynamic head and thereby augmenting the turbine pressure ratio and improving its performance. Since the diffuser is significantly influenced by the flow angles downstream the rotor, the exducer angle was modified to keep the swirl lower and an additional two modifications were carried out that affected the diffuser performance. The diffuser edge was smoothened and a centre body introduced to reduce the recirculation regions and improve its performance. It was found that the static pressure recovery coefficient was increased by 18 percentage points and the relative total pressure loss in the diffuser was decreased by 2.1 percentage points.

Best configuration

An optimum was found when exducer angle was reduced to 45° from 60° and the tongue area was decreased from 290 mm^2 to 270 mm^2. This change combined with the diffuser edge smoothing and centre body application resulted in an improvement in total-to-static efficiency of the system (turbine and diffuser setup) by 4.2 percentage points. The diffuser performance was also significantly enhanced from 7 % to 63 % with a reduced relative pressure loss from 13.3 % to 4.6 %.

1.3 Objectives of the thesis

The parametric trends presented by Sol [2] and Koen [3] establish how the exducer angle and tongue area affect the turbine performance. Although these models aid in establishing a starting point, they are essentially suitable for preliminary design studies and poorly applicable for a thorough design optimization for the MTT radial turbine. Consequently a more accurate design methodology is necessary aiming at:

- Identifying the geometrical and performance parameters for the MTT rotor.
- Performing a 3-D CFD optimization to analyse the parametric trends with respect to turbine performance.
- Performing a 3-D CFD flow analysis of the optimized rotor with the MTT diffuser domain to study in greater detail the effect of the associated swirl losses on diffuser performance. This will also aid in capturing the aerodynamic effects due to the interaction between the optimized rotor and diffuser components.
- Analysing the optimized design solution from a mechanical point of view in order to provide an overview of the changes in stresses associated with the optimized rotor as compared to the current design.

Consequentially the final objective of this study is to increase the turbine efficiency , establish an optimum swirl to reduce its associated loss, and provide adequate stress information for the optimized design solution to aid future work and prototyping.

1.4 Optimization methodology

The flow chart of the optimization process is as shown in Figure 1.1. The first step is assigning the performance parameters for the rotor which is the total-to-total efficiency. The second step is to build the CFD domains for flow analysis. The models are created by parametrizing the rotor geometry using key design variables such as the tip radii(the hub and shroud radii at leading edge), the hub and shroud radii at trailing edge, tip width, axial length and exducer angles. Once the geometry parametrized, it is meshed. Several runs are made to fix mesh settings by performing mesh convergence analysis. These parametric models are then used in the goal-driven optimization component. Using design of experiments, several combinations of parameters at off-design conditions are created as the 'design space'. These design points are analysed by running each case in the fluid analysis component and their output is recorded. A response surface is then constructed by fitting the collected data with arbitrarily complex functions. At this stage, the sensitivity analysis is performed wherein the influence of parameters on the objective function is analysed using the response surfaces in order to eliminate any parameter that has an negligible effect on the output. This is primarily done to reduce the computational time and resources required to achieve the optimization without loss in accuracy. Numerical optimization algorithms are then utilized to obtain the

most efficient rotor geometry. Each of the components and its stages mentioned in this section will be discussed in major detail later in this thesis.

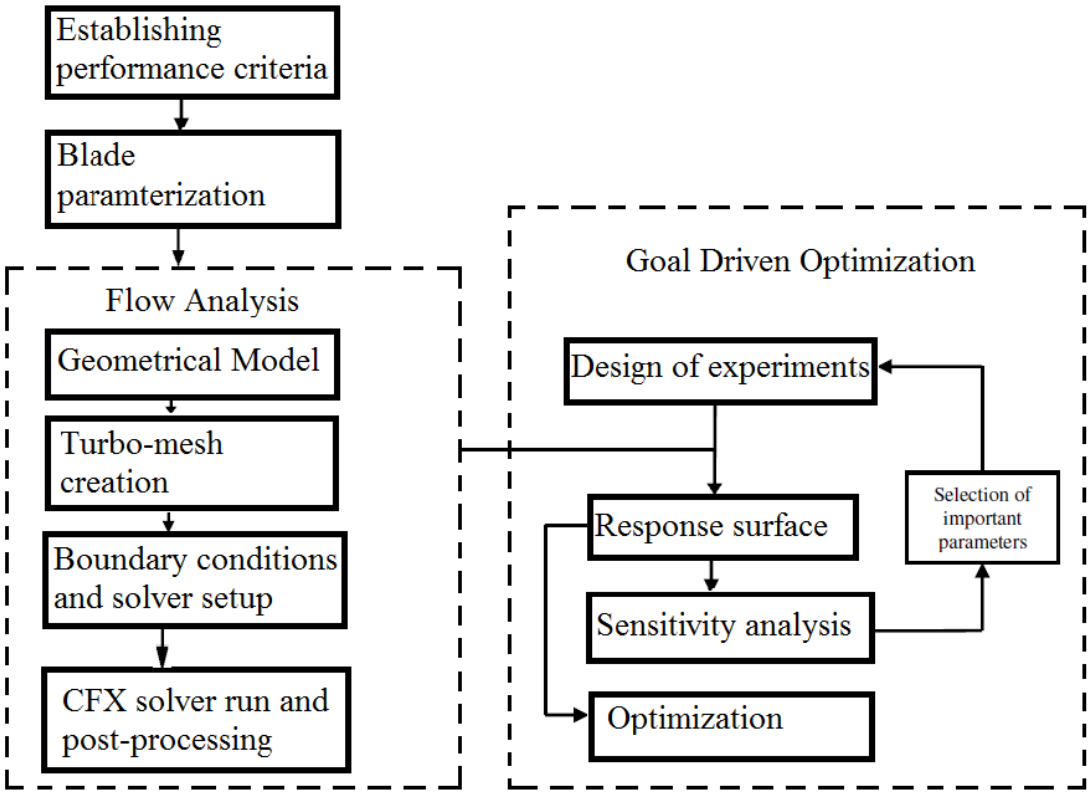

Figure 1.1: Flow chart delineating the steps of the optimization process

Chapter 2

Micro Gas Turbine Technology

2.1 The Brayton cycle

Brayton cycle is a thermodynamic cycle using constant pressure, heat addition and rejection [9]. Atmospheric air is continuously drawn in and compressed to a higher pressure ratio by the compressor and in the combustion chamber, it is mixed with fuel and heat addition takes place and then these hot combustion gases are expanded in the turbine where work is extracted. It can be categorized as either an open or a closed cycle. The difference between the two is that in a closed cycle the turbine exhaust gases are reused at the intake and in an open cycle exhaust gases are not reused. The open and closed cycles are represented in Figure 2.1.

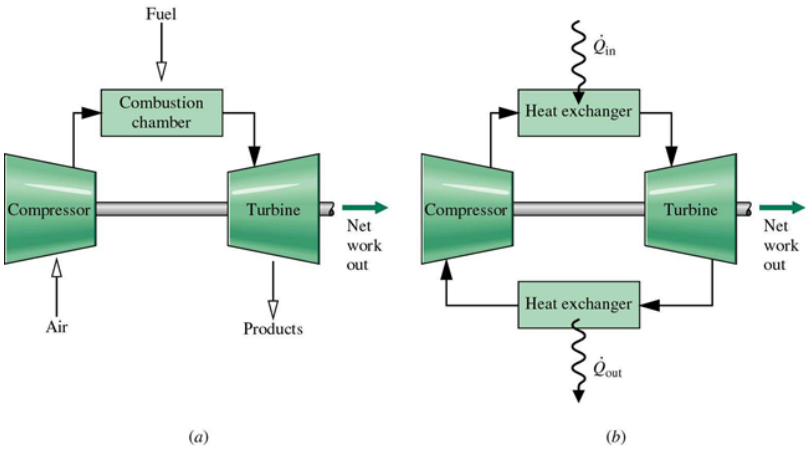

Figure 2.1: Open and Closed Brayton Cycle

2.1.1 Real and ideal cycle

The ideal cycle represents a theoretical case in which the gas exhibits ideal gas behaviour and it does not account for the losses due to heat, pressure, leakage etc. and is represented in Figure 2.2. But in a practical scenario each component of the gas turbine is not performing at 100 % efficiency and the losses should be accounted for. Hence the ideal cycle is adapted and is represented by the real Brayton cycle as shown in Figure 2.3. It is important to note that there is net positive work output because the work retrieved by expansion is more than that required for the compression process due to the diverging nature of the isobars [10].

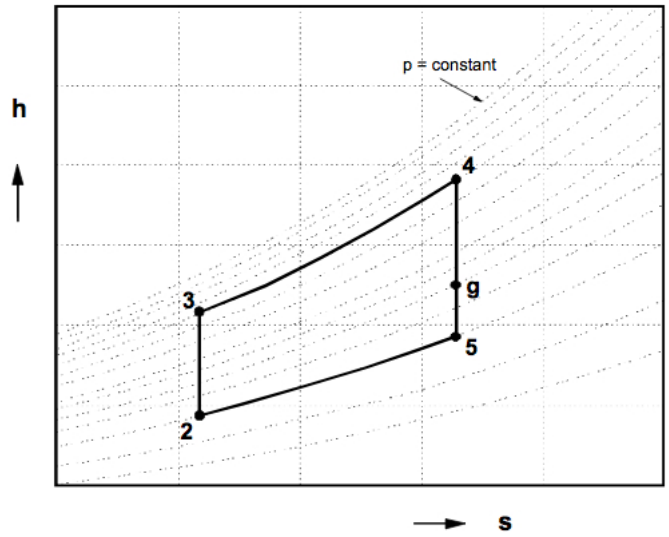

Figure 2.2: The ideal Brayton cycle [9].

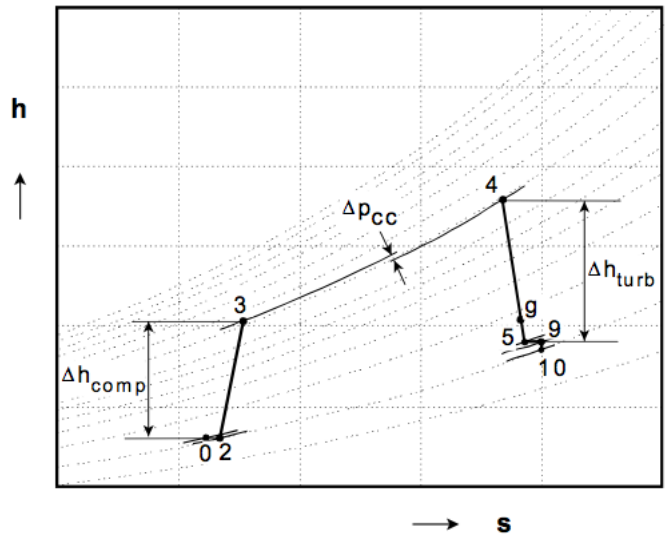

Figure 2.3: The real Brayton cycle [9].

2.1.2 Recuperated Brayton cycle

The primary ways to improve the thermodynamic efficiency of a simple Brayton cycle would be either to increase the work output or to reduce the amount of heat added to the system [11]. The former can be achieved by rotor design optimization and is set to be achieved as part of this thesis objective and the latter can be achieved by recovering the exhaust waste heat of the hot gases leaving the gas turbine or in other words by recuperation and is represented in Figure 2.4. The recovered heat is used to pre-heat the compressed air before further heat addition in the combustion chamber. This leads to a reduction in the heat/fuel input required for the cycle to maintain the required specific power and as a result an enhancement of the thermal efficiency follows. The larger the temperature difference between the turbine outlet section and the compressor outlet section, greater the recuperation but here in lies the major design challenge as the recuperator must be able to cope with high exhaust gas temperatures. Since it essential that the turbine exhaust gases should be hotter than the compressor outlet temperature for recuperation to work, there is a restriction on the pressure ratio. The micro turbines with lower power output inherently work at lower pressure ratios and as a result stand to benefit most from the use of recuperation.

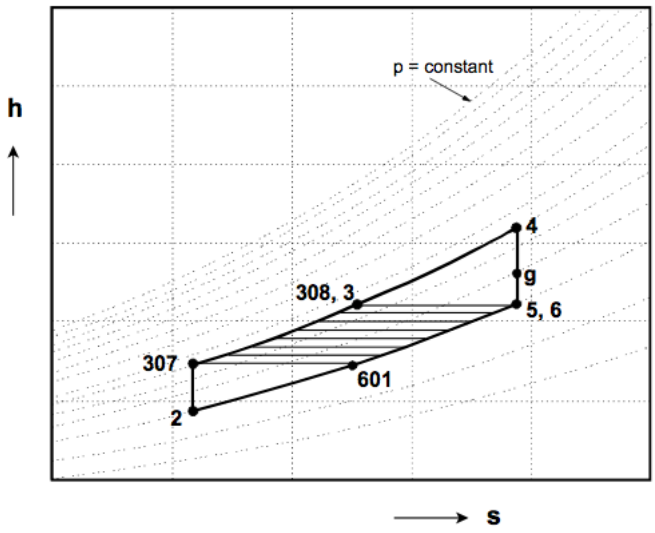

Figure 2.4: The recuperated Brayton cycle [9].

2.2 Micro turbine technological development

Over the past decade, there has been an increasing need for the development of gas turbines with lower power output for CHP applications. The use of micro turbines with the recuperated cycle has therefore seen an upward trend. For such small scale power generation the micro turbines offer significant advantages in terms of performance, noise abatement, CO_2 emissions and also since the waste heat recovered can be used for both domestic and industrial purposes. These micro turbine designs usually comprises of a single stage radial compressor,

a combustor, a single stage radial turbine and a recuperator. This recuperated CHP system is as shown in Figure 2.5.

Micro Turbine Technology B.V. is currently developing a 3 KW recuperated micro turbine for CHP applications. In 2010, the development towards a 12.2 % efficient demonstrator has been described in Visser et al. [6]. Subsequently the performance optimization work was also done to obtain the 18 % turbogenerator electric efficiency target [4]. Development of an efficient turbomachinery optimized for a given cycle is very expensive and a cost effective alternative is using off-the-shelf turbocharger components especially since their technology is already well developed and since they are mass produced. The current MTT Mk6 test setup has an electrical efficiency of about 15.6 % with a turbine inlet temperature(TIT) of about 1300 K, which is much higher than the prescribed OEM design point. Since the MTT turbine operates at an off-design condition, this is not its maximum efficiency. Consequently there lies an interesting opportunity for optimizing the components of the micro turbine to improve its overall efficiency. Within this work the primary focus is on optimizing the high speed radial turbine present in the MTT system. For this purpose high fidelity models and optimization process need to be established and this will be explained in greater detail in the subsequent sections. The next section will present a brief overview of the components and relevant performance parameters necessary for the analysis.

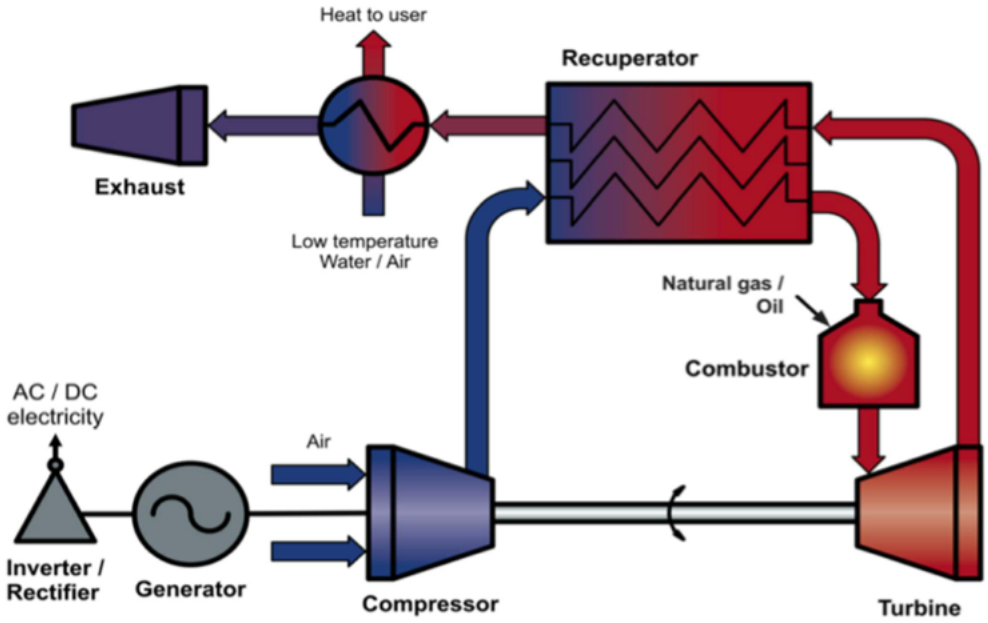

Figure 2.5: Recuperated based CHP system [4].

Chapter 3

Performance of Micro Gas Turbines

This chapter will describe the principal components of the micro turbine involved in this study and their performance characteristics.

3.1 Radial turbine

For turbines with lower power output capability, the use of radial turbines is predominant and the MTT set-up uses a radial inflow turbine. The flow is smoothly oriented at 90° and as a result the radial turbine experiences lesser mechanical and thermal stresses which makes it ideal to use for lower power size applications($< 100\,\mathrm{KW}$).

3.1.1 Principle of operation

The function of the turbine component is to expand the flow downstream the combustor and extract the energy contained in the working fluid and convert it to mechanical or shaft power. In a radial inflow turbine, the flow enters the turbine radially to the shaft and exits along the axis of rotation as shown in Figure 3.1. The working fluid is accelerated across the blade passage and as a result it is expanded and produces a positive power output. The inlet and outlet stations are described using velocity triangles as represented in Figure 3.2.

3.1.2 Volute design

There are two types of enclosures that can be used to deliver the working fluid to the rotor periphery which are the vaneless housing and vaned stators which comprise of a series of angled

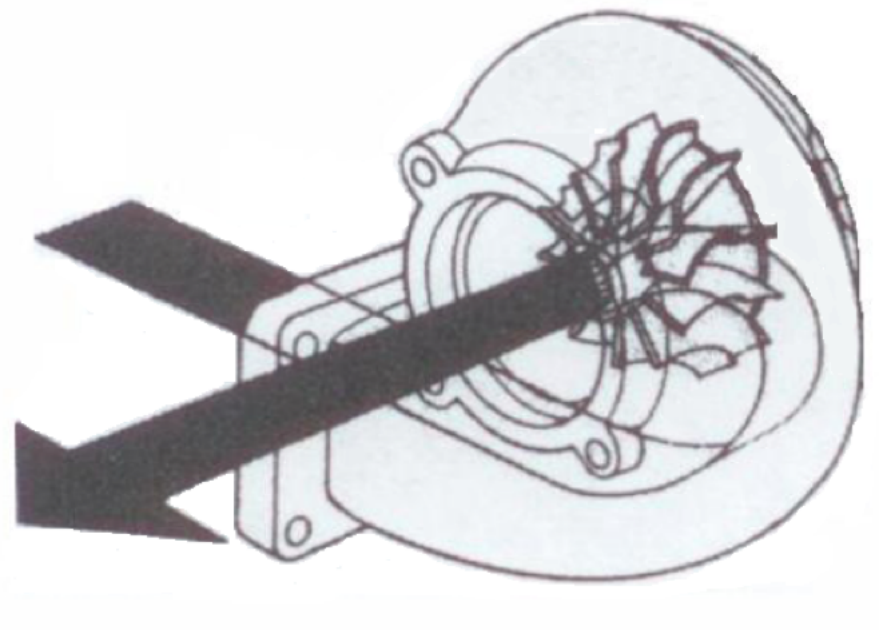

Figure 3.1: Rotor and volute [12].

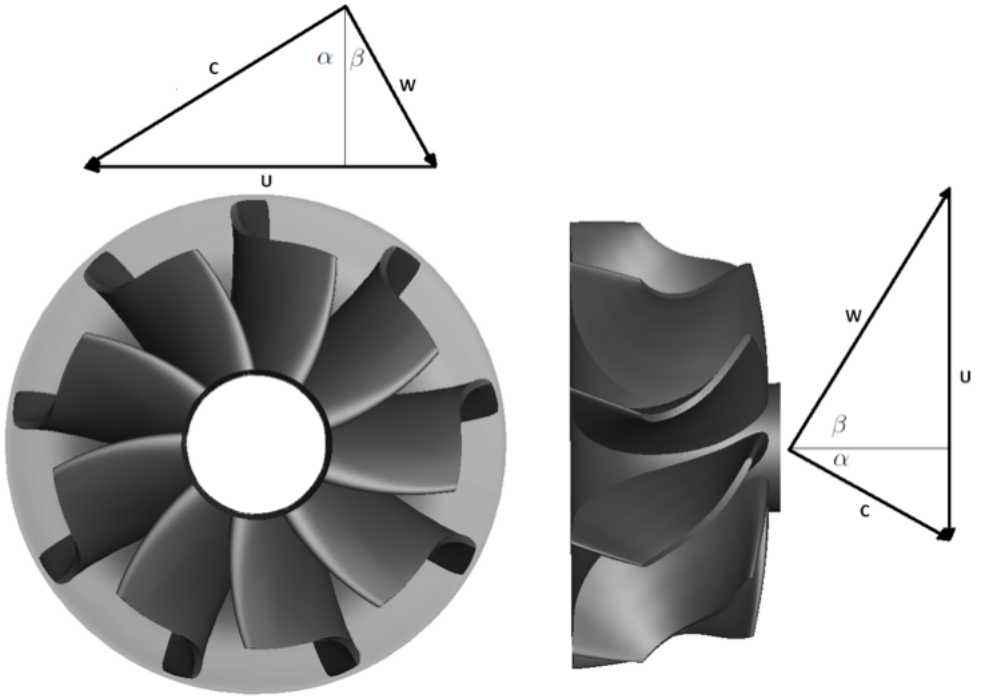

Figure 3.2: Velocity triangles at rotor inlet and outlet [2].

guide vanes [13]. Since it has already been established experimentally and numerically by Simpson et al. [14] that vaneless stators deliver consistent and significant efficiency advantages compared to the vaned stators over a wide range of operating points , the MTT radial turbine

uses a vaneless housing as shown in Figure 3.3. The volute is a vaneless housing whose cross-sectional area is progressively reduced circumferentially in order to provide the desired angular momentum relative to the rotor with minimal stagnation pressure losses. It converts a part of the engine exhaust gas energy from the combustor into kinetic energy and directs the flow towards the rotor inlet i.e. it controls the inlet mass flow to the rotor and the absolute inflow angles [15].

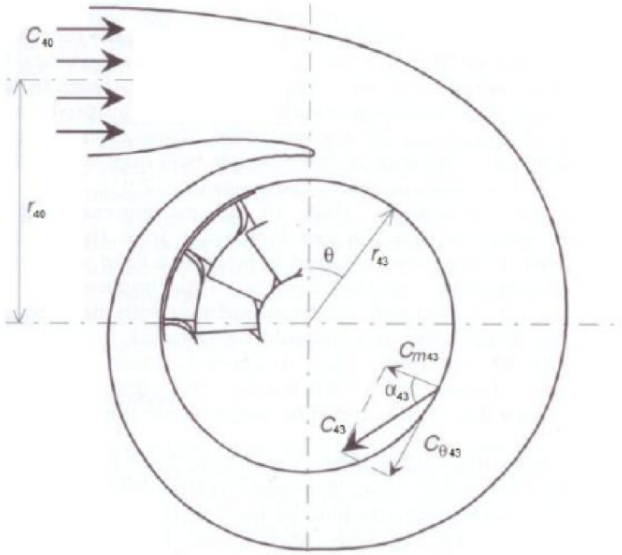

Figure 3.3: Volute Geometry [16].

3.1.3 Performance characteristics

Turbine power

The primary purpose of the turbine is to extract the energy from the working fluid accelerated by the volute and convert it to mechanical work and power output can be computed by using Eq. 3.1.

$$P = \eta_t \dot{m}(h_{04} - h_{05}) \tag{3.1}$$

The total enthalpy difference between the inlet and outlet stations of the rotor can be computed using the Euler turbo machinery equation 3.2. Since the flow is accelerated across the convergent rotor passage, the relative velocity at rotor exit is higher than at inlet and the velocity vector due to rotation is decreased in magnitude at outlet as compared to inlet since the outlet diameter is lower than the inlet for a radial inflow turbine. As a result these factors contribute favourably to the specific work output and also emphasize why radial inflow turbines are generally preferred.

$$\Delta h = (h_{04} - h_{05}) = U_4 C_{\theta 4} - U_5 C_{\theta 5} \tag{3.2}$$

Efficiency

The most important parameter of any expander is the efficiency. There are two main definitions of efficiency which are the the total-to-total efficiency and the total-to-static-efficiency. The predominantly used definition is the total-to-static efficiency since the the dynamic head downstream for most turbine applications can be considered irrecoverable [17]. The MTT system however, has a diffuser downstream of the turbine to recover the dynamic head and hence the usage of the total-to-static efficiency would be misleading. Consequentially it is more apt to use the total-to-total definition of efficiency which assumes the dynamic head as recoverable. The total-to-static and total-to-total efficiencies are represented by Eq. 3.3 and 3.4 respectively.

Although Eq. 3.4 considers that the entire dynamic head is recoverable, in reality only a portion of it can be recovered. The circumferential component of velocity or the swirl component of the dynamic head is not recoverable and should be considered as lost. Hence, the standard total-to-total efficiency will be modified by removing the swirl energy (E_θ) from the definition to more suit this study and to present a higher fidelity model for analysis and optimization. The modified definition is represented by Eq. 3.5. Proceeding further in this thesis, any mention about the radial turbine efficiency refers to $\eta_{tt,5_{ax}}$.

$$\eta_{ts} = \frac{h_{04} - h_{05}}{h_{04} - h_{5,is}} \tag{3.3}$$

$$\eta_{tt} = \frac{h_{04} - h_{05}}{h_{04} - h_{05,is}} \tag{3.4}$$

$$\eta_{tt_{ax}} = \frac{h_{04} - h_{05}}{h_{04} - [h_{05,is} - \frac{(C_\theta)^2}{2}]} \tag{3.5}$$

$$h_{05,is} = h_{04} - c_p T_{04}[1 - (\frac{p_{05}}{p_{04}})^{\frac{\gamma-1}{\gamma}}] \tag{3.6}$$

Rotor exit swirl coefficient

At the exit of the radial turbine the flow has high speeds and a high degree of swirl. The swirl component is a loss and plays a significant role in affecting turbine performance and of the diffuser downstream. Its effect on the performance of these components is complex and will be investigated in detail later in this thesis. The magnitude of the circumferential component of velocity at rotor exit is normalized with the total velocity magnitude at rotor exit, as in Eq. 3.7.

$$N_\theta = \frac{C_{\theta 5}}{C_5} \tag{3.7}$$

Velocity ratio

One term that is often used while representing efficiency of a turbine is the velocity ratio. It is the rotor tip speed normalized with the spouting velocity as in Eq. 3.8. The spouting velocity

is the velocity which will be obtained during an isentropic expansion of the gas between the entry and exit pressures of the stage, see Eq. 3.9. For a radial inflow turbine, usually the maximum efficiency is attained at a velocity ratio in the range $0.68 < \frac{U_2}{C_s} < 0.71$ [18].

$$Velocity\ ratio = \frac{U_2}{C_s} \tag{3.8}$$

$$\frac{C_s^2}{2} = \Delta h_{0,is} = c_p T_{04}[1 - (\frac{p_{05}}{p_{04}})^{\frac{\gamma-1}{\gamma}}] \tag{3.9}$$

Mechanical constraints

A micro turbine operates usually at very high speed of rotation and the MTT turbine runs at 240 krpm [12]. At such high speeds, any change in the diameters that occurs as a result of the optimization is going to change the centrifugal loads significantly. These centrifugal loads are responsible for high stresses and when combined with the aerodynamic loads, they contribute significantly towards reduction in the turbine lifetime and pose a critical constraint while manufacturing. The von-Mises stress or equivalent tensile stress aids in predicting yielding of materials under multi-axial loading [19] and computed as shown in Eq. 3.10. The complete theory behind the von-Mises stress calculation is complex and out of the scope of the current thesis. These values are computed using ANSYS Mechanical and its primary aim is to provide an overview about the difference in stresses between the baseline and optimized design. The modelling of the setup for this analysis and the relevant material properties will be discussed in detail later in this thesis.

$$\sigma_v = \sqrt{\frac{3}{2} s_{ij} s_{ij}} \tag{3.10}$$

where s_{ij} are the components of the stress deviator tensor σ^{dev}.

$$\sigma^{dev} = \sigma - \frac{1}{3}(tr\ \sigma)I \tag{3.11}$$

3.1.4 Limitations

Mass flow mismatch and Choking

The change in rotor geometry that occurs as a result of the optimization will cause a change in mass flow rate through the system and this will lead to a mismatch with other components. Scaling of the turbine could be done to adjust the mass flow rate at the expense of efficiency drop. An alternate solution would be to change the volute tongue area which directly influences the mass flow at rotor inlet.

Choking is a flow condition where the mass flow rate does not increase with further decrease in downstream pressure for a constant upstream pressure. At adiabatic conditions,

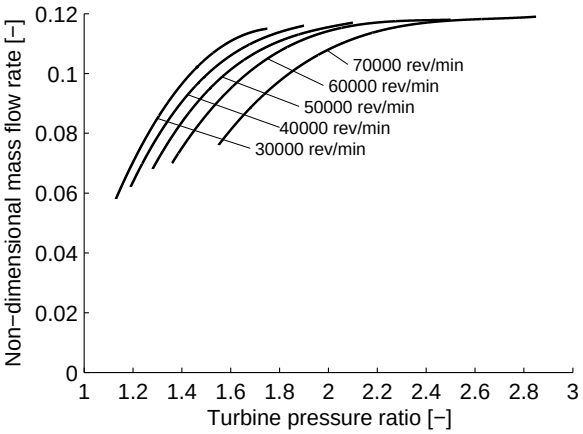

Figure 3.4: Turbine map [20].

this occurs when the velocity reaches sonic conditions and combined with the fact that the upstream density is fixed, there is no increase in mass flow and a maximum limit is reached. Although there are several advantages the volute provides over the vaned stators, in the MTT choking is a drawback as it tends to occur further downstream the rotor instead of the stator. The vaneless stator does not choke the flow like in conventional vaned housings where flow is choked at the stator or the nozzle before the flow enters the rotor. This is done to ensure that the mass flow at rotor inlet is fixed and to prevent any pressure losses due to shock waves that might occur in supersonic expansions. At a given speed of rotation, the mass flow rate does not increase beyond a critical pressure ratio as shown in Figure 3.4. The non-dimensional critical mass flow is define as in Eq. 3.12.

$$\dot{m}_c = \dot{m}\frac{\sqrt{T_{04}/T_{stp}}}{p_{04}/p_{stp}} \tag{3.12}$$

3.2 Diffuser

3.2.1 Principle of operation

The MTT CHP system has an unique diffuser set-up downstream the radial turbine for two specific purposes. Firstly, it is to recover the dynamic head downstream to improve turbine performance. This is accomplished by slowing down the flow and converting the dynamic head into static pressure rise and thereby enhancing the pressure ratio across the rotor stage to get more power output. The second reason is to ensure that the hot gases are transported with minimal pressure losses to the recuperator where the heat can be extracted for further use.

3.2.2 Performance characteristics

Coefficient of static pressure recovery

The performance of the diffuser is evaluated based on the static pressure recovery coefficient which is defined as the ratio between the static pressure difference and the dynamic head at entry, as in Eq. 3.13. Since the purpose of the diffuser is to reduce the static pressure at its inlet to enhance pressure ratio across the rotor, a higher value of C_p indicates that the diffuser performs better.

$$C_p = \frac{p_2 - p_1}{p_{01} - p_1} \tag{3.13}$$

Total pressure loss coefficient

The total pressure loss across the diffuser is identified by using Eq. 3.14. The total pressure difference between the inlet and outlet stations is normalized by the dynamic head at entry.

$$\xi = \frac{p_{01} - p_{02}}{p_{01} - p_1} \tag{3.14}$$

Relative pressure loss

This coefficient is computed to identify the total pressure loss in the diffuser. The total pressure loss across the diffuser is normalized using the total inlet pressure, as in Eq. 3.15.

$$P_L = \frac{p_{01} - p_{02}}{p_{01}} \tag{3.15}$$

Chapter 4

Radial Turbine Modelling

4.1 0-D model

The 0-D model can be used to rapidly establish the turbine performance and the associated losses (e.g. profile, secondary, tip-leakage, and incidence). Even though the 0-D models accuracy has been improved, it is still unable to accurately capture the losses due to swirl and other associated pressure losses especially with change in Mach number beyond transonic conditions. Once the rotor geometry is modified, a Mach number variation is almost certain and this will significantly affect the pressure and swirl loss terms but the 0-D model is only capable of predicting these losses with certainty until a Mach of 0.4, beyond which data has to be extrapolated and its loses accuracy significantly. The 3-D flow phenomena such as boundary layer separation, turbulence associated effects are especially pronounced in the currently turbo machinery application due to its small scale and high speeds. As a result, highly efficient turbine design can be achieved only through a high fidelity CFD simulation.

4.2 3-D blade parametrization

Once the performance parameters are established, the next step is parametrizing the rotor geometry to establish the design variables for the optimization. From the earlier studies conducted by Sol [2] and Gideonse [3], two parameters have been established: the exducer angle and the tip diameter. To analyse the effect of the afore mentioned swirl component in Section 3.2 on rotor and diffuser performance, the exducer angle is established as a key parameter. In the previous work, analysis has been conducted with a uniform exducer angle profile along the span but for the optimization in this thesis however, the exducer angles at the shroud and hub stations are used as parameters to analyse the effect of this parameter on both rotor and diffuser performance in greater detail. The variation in tip radii at the

shroud and hub regions though less in magnitude is taken into account for the optimization and consequently comprises of two separate parameters to define it: the leading edge hub radius and the leading edge shroud radius. The other vital radial parameters considered for optimization as part of this work include the trailing edge radius at the hub and shroud region based on the works of Mueller et al. [21] and Aungier [13]. The tip width and the axial length have also been taken into account implicitly as they are incorporated as a function of the other radial parameters mentioned above due to the inherent geometry constraints present in ANSYS Blade Modeller. The list of design parameters are represented in Table 4.1. Figure 4.1 represents a visualization of the rotor geometrical parametrization in the meridional view and Figure 4.2 represents a visualization of the exducer angles.

Parameters		**Definition**
Design parameters		
$R_{hub,te}$	$[mm]$	Trailing edge hub radius
$R_{shroud,te}$	$[mm]$	Trailing edge shroud radius
$R_{hub,le}$	$[mm]$	Leading edge hub radius
$R_{shroud,le}$	$[mm]$	Leading edge shroud radius
β_{hub}	[deg]	Exducer angle at hub
β_{shroud}	[deg]	Exducer angle at shroud
b_{le}	$[mm]$	Tip width (implicit)
Z_{ax}	$[mm]$	Axial length (implicit)

Table 4.1: Design parameters for optimization

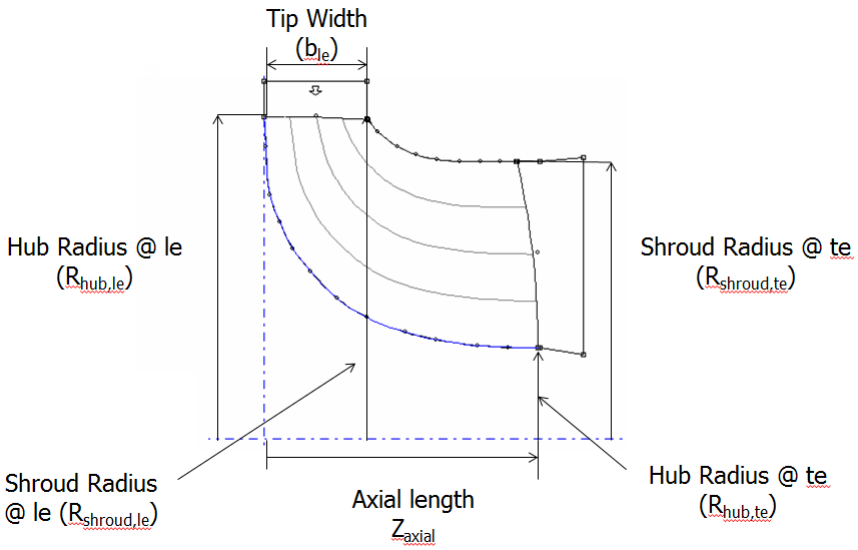

Figure 4.1: Rotor geometry parametrization

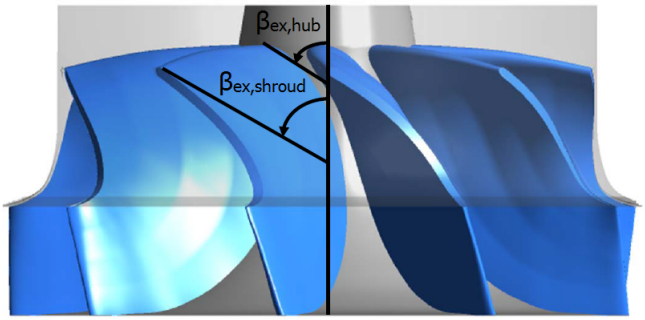

Figure 4.2: Exducer angles

4.3 Turbulence modelling

There are several classes of turbulence models used to predict the fluctuations due to the inertial forces in a fluid. The most predominant ones as elaborated by Wilcox [22] include:

- Direct Numerical Simulation (DNS)
- Large Eddy Simulation (LES)
- Detached eddy simulations and other hybrid models (DES)
- Reynolds Averaged Navier Stokes (RANS)

In theory, the established Navier-Stokes equation can be used to solve flow phenomena which are both laminar and turbulent. However for flows at high speeds, the turbulence length and time scales necessary are smaller than the smallest possible finite volume mesh size which can be used practically for numerical analysis. Hence a highly accurate solution would require using a DNS which solves the Navier-Stokes equation for the entire spatial range of turbulence length and time scales. The major downside however is that it requires a tremendous amount of computing power. The LES models on the other hand solve only for large scale turbulence structures and only implicitly account for the small scale variations. The RANS is a statistical model in which the equations represent only mean flow quantities and it does not resolve the turbulence fluctuations. Though the accuracy of the RANS model is lesser than the others mentioned above, the computational time and resources required for a reasonable flow estimation are within acceptable levels as verified by Spalart [23]. The DES model is a hybrid one which uses the LES model in the bulk of the fluid and RANS model for near wall treatment. The main focus of this thesis is to provide a quantitative overview about the performance parameters of the turbomachinery component used for CHP applications and hence the RANS model is the best suited to achieve the goals of the study at a reasonable computational cost.

The effect of turbulence can be predicted to a certain extent without having to recourse to an extremely fine mesh close to the wall region by the use of wall functions in statistical turbulence models. Since the RANS model averages out the effect of turbulence, it requires

extra transport equations to represent the turbulent flow properties. There are several RANS models which use different wall functions to compute the Reynolds stresses and the two equation models have become the standard for industrial applications and especially for modelling miniature radial turbines now a days [24]. Since these are some of the most accurate RANS models available, they are incorporated for the turbine modelling in this thesis and are discussed in greater detail in the ensuing section.

4.3.1 Two-Equation liner eddy viscosity models

These models use two extra transport equations to predict the mean turbulent properties of the flow. They are based on the Boussinesq eddy viscosity assumption which portrays the effect of the turbulence in the same way molecular viscosity affects the laminar flow [25]. This is accomplished by characterizing the turbulence using scalar variables such as:

- The turbulent kinetic energy (k) to correlate with the more complex turbulence intensity.
- Either the turbulence dissipation energy (ϵ) or the turbulence frequency (ω) to correlate with the turbulent length scales.

Based on these variables, the most widely used models to simulate mean flow characteristics as elaborated by Menter [26] include the k-ϵ, the k-ω and the k-ω Shear Stress Transport(SST) models.

The k-ϵ model

As mentioned earlier the k-ϵ model introduces two new variables into the system of equations, the variance of the fluctuations in velocity or the turbulent kinetic energy (k) and the turbulence eddy dissipation (ϵ) or the rate at which these velocity fluctuations dissipate. This is one of the most validated and simplest models tailored specifically for low pressure gradient free shear flows. While accuracy is reasonable for these planar shear layer flows at high Reynolds number, it poorly predicts the turbulence characteristics for flows with large adverse pressure gradients where boundary layer separation might occur. The prediction is also inaccurate in cases which have rotating flows such as in compressors and turbines, unconfined flows, non-circular ducts etc. [27].

The k-ω model

This model makes use of the same k term but uses a different length scale for turbulence i.e. the turbulent eddy frequency (ω). The major drawback of the k-ϵ model is that it predicts the onset of separation too late and under predicts the magnitude of separation later on. This type of overly optimistic prediction makes it necessary to incorporate complex damping functions for improving accuracy. The k-ω model on the other hand requires much lesser near

wall resolution which allows a smooth shift from a low Reynolds number form to wall function formulation and thereby gives a better prediction of separation under adverse pressure gradients than the k-ϵ model.

The k-ω SST model

Though the k-ω enhances the prediction of the boundary layer phenomena, it experiences strong free- stream sensitivity in its ω values and its prediction is inaccurate for free-shear flows. The shear stress transport model on the other hand combines the best aspects of both the k-ϵ and k-ω models and can be used without incorporating any complexity due to additional damping functions. Since it incorporates the k-ω formulation in the inner parts of the boundary layer and switches to a k-ϵ behaviour in the free-stream, it avoids the common k-ω problem that the model is too sensitive to the inlet free-stream turbulence properties. The turbomachinery application at hand has a high degree of rotational flow along with adverse pressure gradients and is expected to experience boundary layer separation, the k-ω SST model with it superior prediction accuracy is adopted as a result.

4.4 Rotor mesh

4.4.1 Fluid domain

The fluid domain of the rotor is meshed using ANSYS TurboGrid in which a structured hexahedral mesh is created using the ATM optimized method. In order to ensure compatibility with the k-ω SST model used in the CFX solver, the mesh elements closer to the wall have a y^+ value of the order of unity. For the mesh sensitivity analysis plots shown below, the boundary conditions specified are as represented in Table 4.2. From Figure 4.3, it can be observed that the both the mass flow rate and efficiency are not predicted well for the coarse mesh. The mass flow rate converges to a value around 65.5 g/s for 1 million or more elements. The efficiency on the other hand converges at around 1.5 million elements to a value of 78.1 %. Consequently, it is chosen to have a rotor mesh with 1.608.608 elements for achieving reliable predictions at a reasonable computational cost.

Boundary Conditions		**Value**
Total Inlet Temperature	$[K]$	1285
Total Inlet Pressure	$[bar]$	2.82
Static Outlet Pressure	$[bar]$	1.021
Speed of Rotation	$[rpm]$	240000

Table 4.2: Boundary Conditions for rotor domain only simulation

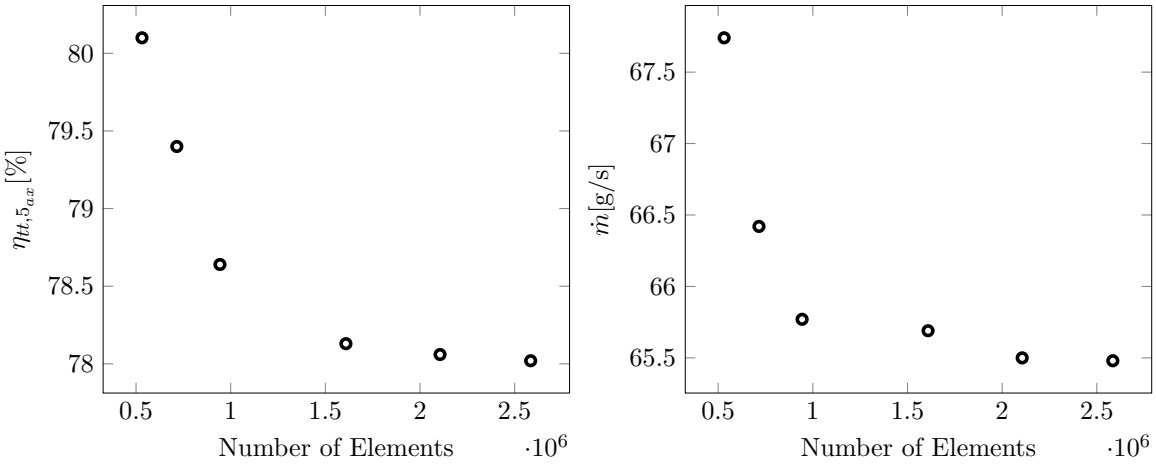

Figure 4.3: Rotor fluid domain mesh sensitivity for efficiency and mass flow

4.4.2 Solid domain

For mechanical modelling, a solid domain of the rotor including its hub and shaft are necessary. The symmetry of the rotor makes it possible to model just a 40° sector. An unstructured tetrahedral mesh is created with the default meshing software in ANSYS Workbench. The aerodynamic loads are imported from the CFX solver simulations mentioned above and a rotational speed of 240.000 rpm is specified for the shaft. The sensitivity analysis to determine the mesh size is done against the maximum and minimum Von-Mises stresses. From Figure 4.4 , it can be observed that the maximum Von-Mises stresses converge to a value of around 1608.3 MPa at 80.000 elements or more. The minimum stresses are predicted accurately even with a coarser mesh. Therefore for the mechanical analysis of the rotor domain, a mesh with 78.716 elements is chosen since it provides reliable stress prediction at a reasonable computational cost.

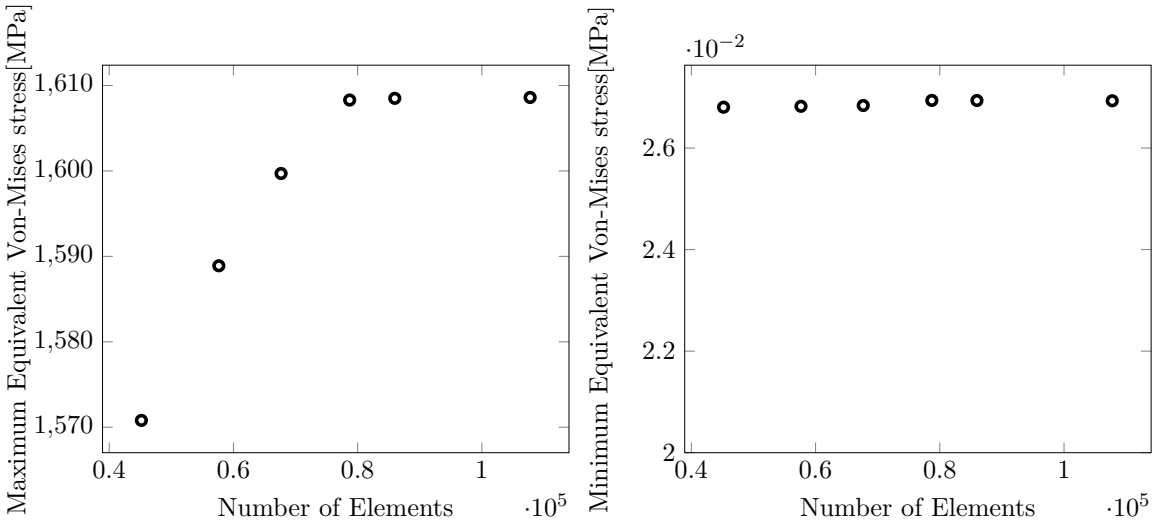

Figure 4.4: Rotor solid domain mesh sensitivity for efficiency and mass flow

4.5 Diffuser mesh

The MTT diffuser domain is unique and non-axisymmetric and consequently the entire domain needs to be modelled. An unstructured tetrahedral mesh is created with a structured hexahedral mesh close to wall to capture boundary layer effects. For the sensitivity analysis, the mesh is coupled with the rotor domain and the boundary conditions are as specified in Table 4.3. For determining the optimal mesh size, the effect on the total-to-static efficiency $\eta_{ts,9}$ and pressure recovery coefficient C_p for the diffuser are analysed. From Figure 4.5, it can be observed that efficiency converges to a value of around 63.5 % and the pressure recovery to about 30 % for 1.5 million diffuser mesh elements or more. Hence the final setup comprises of a diffuser mesh with 1.531.430 elements to achieve reliable predictions at a reasonable computational burden.

Boundary Conditions		**Value**
Total Inlet Temperature	$[K]$	1285
Total Inlet Pressure	$[bar]$	2.82
Static Outlet Pressure	$[bar]$	1
Speed of Rotation	$[rpm]$	240000

Table 4.3: Boundary Conditions for simulation with diffuser domain

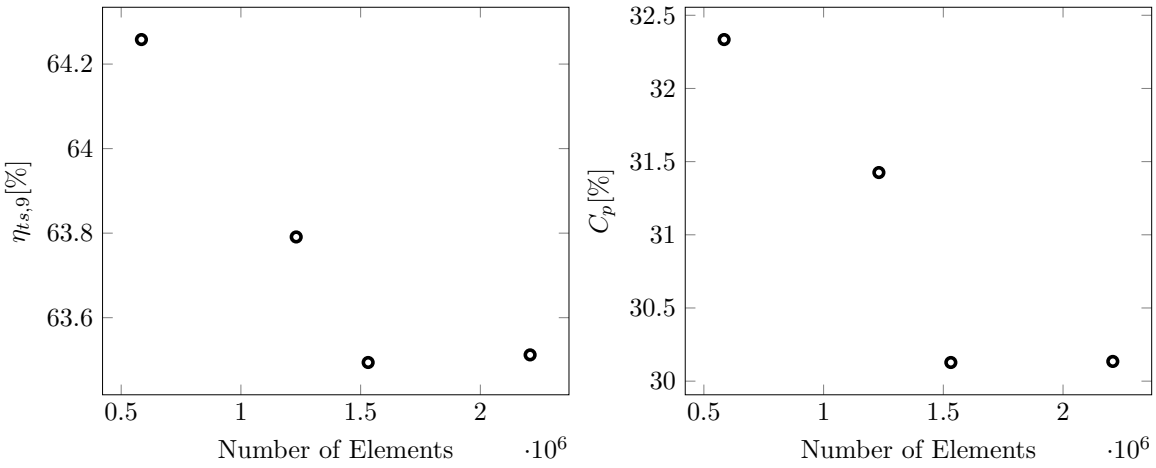

Figure 4.5: Diffuser domain mesh sensitivity for efficiency and pressure recovery

4.6 Solver setup

In the previous section, mesh settings for the baseline rotor and the diffuser have been established and the next step is setting up the ANSYS CFX solver. The final fluid domain setup will comprise of a rotor with 1.608.608 elements and a diffuser with 1.531.430 elements. The rotor and diffuser meshes are as represented in Figure 4.6 and Figure 4.7 respectively. Both these meshes have a y^+ value of the order of unity to ensure accurate near wall resolution.. Since the optimization process is carried out only for the rotor, the inlet domain is expanded as shown in Figure 4.6 to prevent any back flow that might occur if the domain is too small. There are two options for the steady state interface settings between the rotor and diffuser domain : mixing plane and the frozen rotor interface. The mixing plane model circumferentially averages the variables at the interface whereas the frozen rotor interface fixes the rotor position at a particular rotation angle and this position would significantly affect the outcome of the simulation. Moreover the uses of such interface makes the simulation more expensive. Consequently a steady k-ω SST model with a mixing plane between the rotor and the diffuser domains is adopted to provide reliable predictions at a reasonable computational cost. The boundary conditions for the simulations include: total inlet pressure, total inlet temperature and static outlet pressure. In both cases with and without the diffuser domain, the rotor speed is fixed at at 240 000 rpm and the walls are modelled as adiabatic, smooth, no slip walls.

Since the rotor is subjected to high pressures and temperatures of close to 1300 K, the material used must be suited for service in such extreme environments. INCONEL 713C is used to manufacture the MTT rotor since these alloys are oxidation and corrosion resistant materials which retain strength over a wide range of temperatures making them inhibit creep effectively. The material properties of INCONEL-713C from [28] used for the mechanical analysis are represented in Table 4.4. The solid domain mesh is represented in Figure 4.8. ANSYS Mechanical is used for structural analysis. The translational motions of the shaft are fixed and it possesses only rotational degree of freedom about the coordinate Z-axis with a specified speed of 240 000 rpm. The rotor is axis symmetric, consequently only a 40° is modelled and the symmetry faces are specified. The aerodynamic loads are imported using the pressure data from the CFX solver. The Equivalent Von-Mises stresses are then extracted for further analysis.

Constants		
Density	$[kg/m^3]$	7913
Coefficient of thermal expansion	$[K^{-1}]$	0.0000106
Reference Temperature	$[K]$	366
Isotropic Elasticity		
Young's modulus	$[MPa]$	206000
Poisson's ratio	$[-]$	0.3
Tensile yield strength	$[MPa]$	800
Tensile ultimate strength	$[MPa]$	1043
Reference Temperature	$[K]$	298.16

Table 4.4: INCONEL 713C material properties

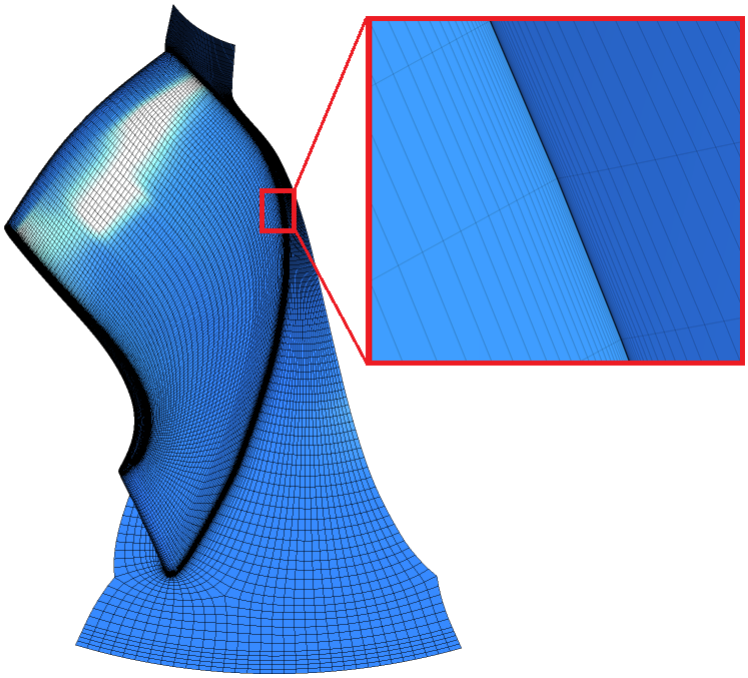

Figure 4.6: Rotor fluid domain mesh

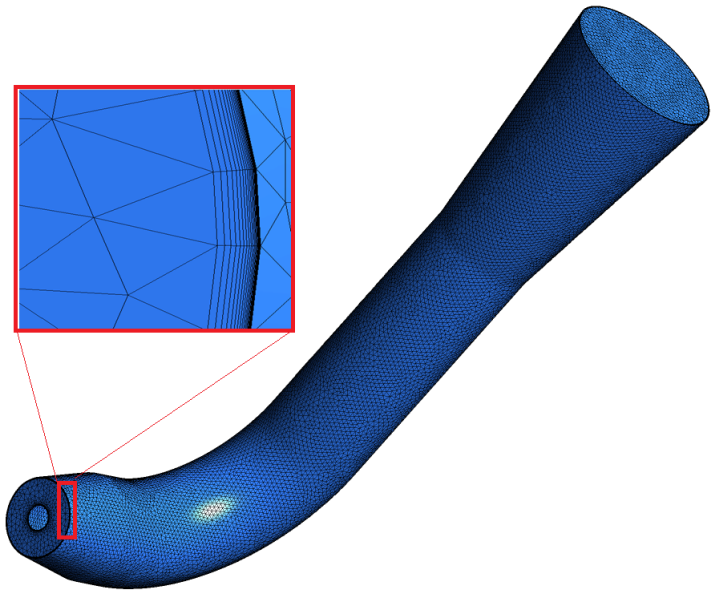

Figure 4.7: Diffuser mesh

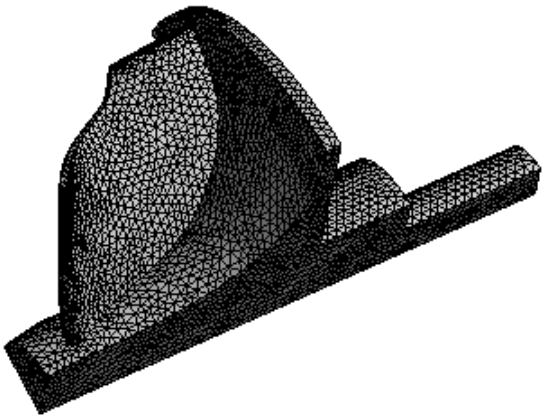

Figure 4.8: Rotor solid domain mesh

Chapter 5

Goal Driven Optimization

This sections presents the goal-driven optimization algorithm which has been chosen to maximize the efficiency of the MTT turbine. The various stages such as design of experiments, the response surface generation from the design space are explained in detail. This is followed by a description about the various numerical optimization methods selected for usage in this thesis and the limitation of the goal driven optimization process.

5.1 Design of experiments

The design of experiments aims at spanning the entire range of admissible values of the design variables. It is used to generate the design space from which the response surface can be built i.e. it computes the output response at specific off-design conditions to aid in establishing parametric trends without the need to analyse all possible combination of input parameters. This is called a fractional factorial design [29]. There are several models that exist for establishing the appropriate design points based on a fractional factorial design, the primary ones include: the central composite design (CCD), box-behnken design, optimal space filling design (OSFD). The box-behnken model avoids computation at the extrema of the design space and is discarded for usage in this thesis. The CCD model on the other hand does not produce a well distributed design space and it can be used only for preliminary analysis [30]. The OSFD fills the design space most efficiently and it creates the best spread out design space. Consequently it is less expensive and responds well with higher order response surfaces and as a result it is selected in this work. With the OSFD, the design type chosen is the Maximum Entropy type as it provides better result prediction for highly correlated design space such as this even although it is computationally more expensive than the Max-Min Distance type and the Centered L2 type. The samples type computes the number of design points the algorithm should generate and the CCD type is used as it generates more design points which allows better meta-model generation later on. It is worth

to note here that the OSFD is used to generate same number of points as a CCD type, the CCD model is not chosen for the design of experiments.

5.2 Response surface and parametric sensitivity

Once the output parameters are computed for all design points by means of the design of experiments, the response is created by fitting the output parameters using regression analysis techniques. A sample response surface as a function of two variables is shown in Figure 5.1. A response surface can be approximated by a first order or second order model depending on whether the response is a linear or non-linear function of the independent variables. In most of the practical applications, the variation is non-linear and a higher order model is required.

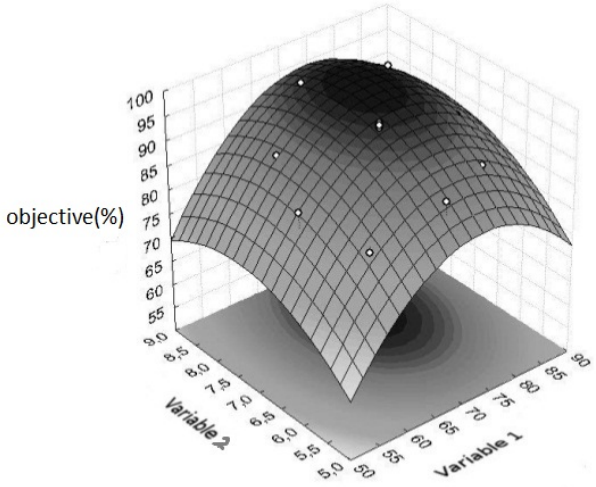

Figure 5.1: Hypothetical response surface as a function of two variables [32].

The response surfaces are developed using regression analysis techniques. Regression analysis is a statistical methodology that utilizes the relationship between two or more quantitative variables (independent variables) so that the dependent variable can be estimated from them. The common regression models for response surfaces include : standard response surface(2^{nd} order polynomial), non-parametric regression (NPR), Kriging and neural network. A p-degree polynomial regression model as presented by Anthony [31] is shown in Eq.5.1,where y is the dependent variable and x is the independent/predictor variable. In a standard response model, p=2. For higher order polynomials(p>2), the Kriging and the NPR are the most accurate. NPR belongs to a general class of support vector method type techniques which employ data classification methods which use hyperplanes to separate data groups. The hyperplane is used to categorize a subset of the input sample vectors called support vector set which are deemed sufficient to represent the output in question [33]. The NPR does not provide auto-refinement capabilities and is used only when fit metrics of the response surface is unsatisfactory. The Kriging option on the other hand provides a more accurate multidimensional interpolation

which combines a polynomial model similar to the one of the standard response surface to provides a global model of the design space along with local deviations. Moreover, a detailed goodness of fit report describing the accuracy of the complex polynomial fit is also provided. The effectiveness of the Kriging algorithm is based on the ability of its internal error estimator to improve response surface quality by generating refinement points and adding them to the areas of the response surface most in need of improvement [34]. Consequently, the Kriging meta model was used in this thesis. For efficiently utilizing the computational resources, it is essential to minimize the number of initial design parameters by establishing and using only those parameters that affect the objective function chosen(turbine efficiency) significantly. Consequently a sensitivity analysis is carried out in ANSYS Workbench and is explained in greater detail in the ensuing chapter.

$$y = \alpha_0 + \sum_{i=1}^{k} a_{1,i} x_i + \sum_{i=1}^{k} a_{2,i} x_i^2 + ... + \sum_{i=1}^{k} a_{p,i} x_i^p + \epsilon \tag{5.1}$$

5.3 Optimization

Optimization problems are generally either constrained or unconstrained. Unconstrained problems have an objective function with, theoretically, no limitation on the value of the design variable . The goal driven optimization problem in the thesis however is a constrained one with the objective of maximizing the efficiency. These constraints impose limits on the design variables. There exists several algorithms to solve an optimization problem and the review of all of these numerical methods is beyond the scope of this thesis. Instead the focus is on a brief description of the algorithms being implemented in this thesis. Since there is just one objective function(efficiency), two techniques are employed for optimization in this thesis to study the dependency of the final solution on the optimization algorithm. They are the non-linear programming by quadratic lagrangian (NLPQL) and the multi-objective genetic algorithm (MOGA). The NLPQL is a sequential quadratic programming method which solves problems with smooth continuously differentiable objective function and constraints. The algorithm uses a quadratic approximation of the Lagrangian function and a linearisation of the constraints [35]. One of the drawbacks of this algorithm is that it can be used only for continuous input parameters and for solving problems with one objective function. This method solves constrained non-linear programming problems of the form:

$$\begin{aligned} &Maximize: \\ &\qquad y(x) \\ &Subjected\ to: \\ &\qquad g_j(x) \leq 0 \ j = 1, ...m \\ &\qquad x_i^l < x_i < x_i^u \ i = 1, ..., n \end{aligned}$$

The multi-objective genetic algorithm on the other hand is a hybrid variant of the NSGA-II (Non-dominated Sorted Genetic Algorithm-II) based on controlled elitism concepts [36] and as the name suggests, it can be used for either single or multiple objective functions

and it supports all types of input parameters. They are a class of evolutionary algorithms that use techniques inspired by evolutionary biology such as inheritance, mutation, selection, and crossover [37]. The evolution usually starts from a population of randomly generated individuals and happens in generations. In each generation, the fitness of every individual in the population is evaluated, multiple individuals are selected from the current population and modified to form a new population which are a blend of best properties of its parents resulting in a superior subset. The new population is used in the next iteration of the algorithm and the process goes on till the maximum allowable pareto percentage or the maximum number of iterations is reached. From the optimized design obtained from these two algorithms, the best design is then selected and analysed further.

5.4 Limitations of goal driven optimization

One of the major drawback of GDO is the limitation of the number of input parameters that can be used. At the design of experiments stage, the number of design points are generated based on the DOE algorithm chosen and they increase exponentially with the number of parameters. This trend for a fractional factorial design method is shown in Figure 5.2. This is the primary reason for performing sensitivity analysis in order to eliminate any design parameters that does not significantly impact the output. For a design optimization involving more than 10 parameters the cost of optimization increase abruptly. Therefore this method is only appropriate for designs with less than 10 input parameters.

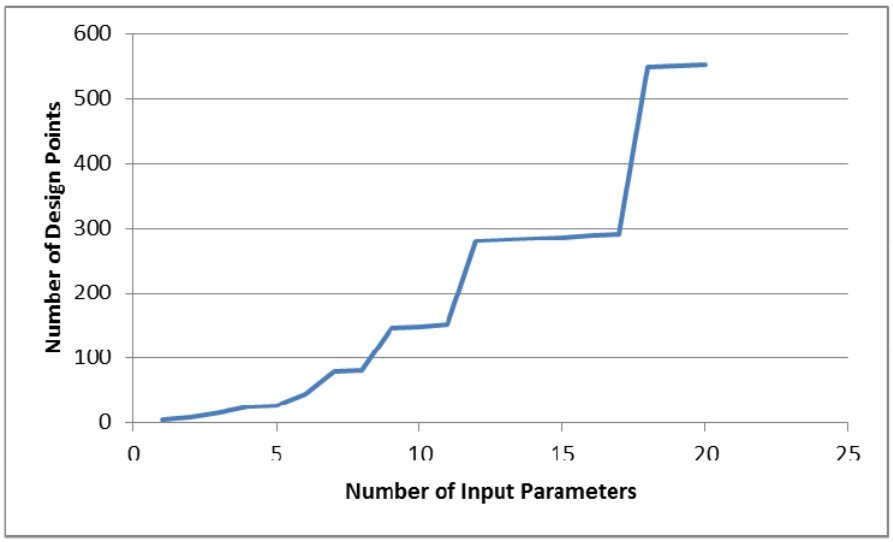

Figure 5.2: Number of design points to number of input parameters [32].

Chapter 6

Multi-Parametric Optimization and Analysis

In this chapter, a multi-parametric optimization is performed. Only the rotor geometry is optimized in order to save computational time and resources. The baseline geometric parameters and its performance characteristics are established in Section 6.1. This is followed by a parametric sensitivity analysis done to eliminate redundant parameters in Section 6.2. The NLPQL and MOGA methods are used to optimize the rotor and the optimal candidate solutions obtained from these algorithms are presented in Section 6.3 along with the verification data. The verification is done to check the consistency of the optimization model with that of the fluid domain simulations. Section 6.4 involves a in-depth analysis of the improvement in performance characteristics of the optimized candidates presented in the previous section. The last section presents the results of the simulations of the optimized candidates with the diffuser domain.

6.1 Reference model simulation

The first step before performing the optimization is establishing the baseline characteristics. A reference model simulation is set-up using a steady state k-ω SST model as mentioned in Chapter 4. The simulations are performed with a total inlet pressure of 2.82 bar, total inlet temperature of 1285 K, a static outlet pressure of 1.021 bar and a rotational speed of 240 000 rpm. The baseline design and performance parameters are shown in Table 6.1. The first 6 parameters are the design variables and the tip width, axial length are incorporated as a function of these parameters. From this, it is apparent that the exit swirl is high and from the previous studies, it is known that reducing the exducer angle would lead to a reduction of this swirl. However the optimum design and the influence of other design variables on

efficiency and the swirl is still unknown and will be investigated in the ensuing sections.

Parameters		Definition	Value
Design parameters			
$R_{hub,te}$	$[mm]$	Trailing edge hub radius	4.83
$R_{shroud,te}$	$[mm]$	Trailing edge shroud radius	14.75
$R_{hub,le}$	$[mm]$	Leading edge hub radius	17.11
$R_{shroud,le}$	$[mm]$	Leading edge shroud radius	16.95
β_{hub}	[deg]	Exducer angle at hub	60
β_{shroud}	[deg]	Exducer angle at shroud	60.18
b_{le}	$[mm]$	Tip width	5.53
Z_{ax}	$[mm]$	Axial length	14.68
Performance parameters			
$\eta_{tt,5_{ax}}$	[%]	Efficiency	78.13
N_θ	[-]	Swirl coefficient	0.5056
$\dot{m}$	$[g/s]$	Mass flow rate	65.69
E_θ	$[J/Kg]$	Swirl energy	25200

Table 6.1: Baseline characteristics

6.2 Parametric sensitivity

The first run of the design of experiments component generates a design space with 45 design points evenly spread out through the specified domain and based on constraints specified for the design variables. The design space generation takes approximately 3 days on a HP workstation with 16 GB RAM and an 8-core Intel Xeon W5590 processor running at 3.33 GHz. The time for the entire procedure is estimated based on how long it takes to generate every design point since ANSYS does not provide the user with this data. The generation of the Kriging response surface is initialized from these design points and the goodness of fit metrics is examined to determine whether the response surface needs refinement. A good response surface fit is observed once an auto-refinement of 8 points is carried out and then the sensitivities are examined. This sensitivity analysis for the design parameters is carried out in order to eliminate any parameter that does not affect the efficiency sufficiently. Figure 6.1a shows the sensitivity of efficiency to the input design parameters. It can be observed that all of the chosen parameters have a significant influence over the efficiency and none of them can be disregarded. The exducer angle is a key parameter in determining the rotor exit velocity and consequently it considerably effects the efficiency (defined by Eq. 3.5) followed by the tip diameters. From Figure 6.1b it can be observed that all the input parameters exert an effect on the swirl and cannot be disregarded. Similar to the case with efficiency, the swirl factor is primarily dictated by the exducer angle. From this study, we can conclude that all of the six parameters, namely: the tip radii(the hub and shroud radii at leading edge), the hub and shroud radii at trailing edge and exducer angles at hub and shroud are significant factors that affect the efficiency and must be taken into consideration over the optimization. Moreover the use of six parameters is well within the bounds of the limitation for the goal driven optimization process as described in Section 5.4. Hence, the optimization

can be performed without incurring any computational overload.

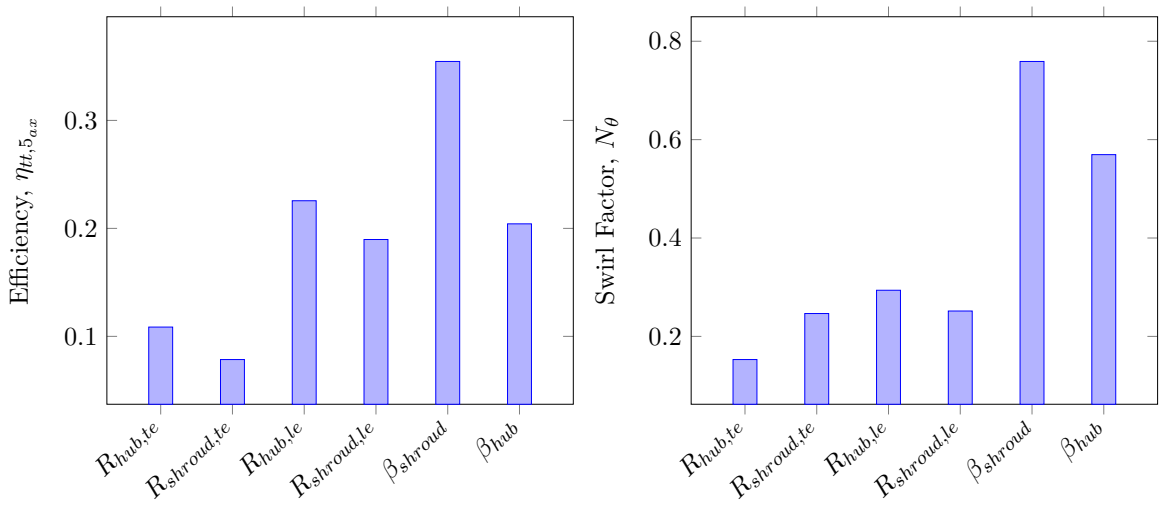

(a) Efficiency **(b)** Swirl factor

Figure 6.1: Sensitivity of performance functions to input parameters

6.3 Optimization

In this section, the results from the optimization using the MOGA and NLPQL algorithms mentioned in Section 5.3 are presented. It is essential to note that the optimal candidates presented by these optimizers are extrapolated from the response surfaces and actual CFD simulations are not performed for these candidates. Hence it is essential to perform a-posterior simulation in order to ensure the accuracy of the optimization process.

6.3.1 MOGA candidates

The multi-objective genetic algorithm has been set-up with the criteria for maximizing the rotor efficiency. The initial optimization run, provided candidate points where there was a discrepancy between the real and approximate fitted model. Since the accuracy was not sufficient, the response surface was refined further using these initial candidate points. The primary performance parameters of interest are the rotor efficiency and the swirl. Consequently the verification is conducted for these objectives. The final optimal candidate points after refinement of response surface and verification are shown below in Table 6.2. The deviation of the results predicted by the optimizer and the actual simulation results are shown in Figure 6.2. Figure 6.2a represents the efficiency verification data and Figure 6.2b represents the swirl verification data. It is apparent that the optimizer over-predicts the values as compared to the simulations of the optimized design points from ANSYS CFX. Since the difference in values of the performance functions is within an allowable limit ($< 1.5\,\%$), the optimizer accuracy is sufficient to achieve the objectives of this thesis.

	$R_{hub,te}$ $[mm]$	$R_{shourd,te}$ $[mm]$	$R_{hub.le}$ $[mm]$	$R_{shourd,le}$ $[mm]$	β_{hub} [deg]	β_{shroud} [deg]	b_{le} $[mm]$	Z_{axial} $[mm]$	N_θ [-]	$\eta_{tt,5_{ax}}$ [%]
Objectives										Maximize
Baseline configuration	4.830	14.75	17.11	16.95	60	60.18	5.53	14.68	0.5056	78.13
Optimal design points										
Candidate A	4.770	14.356	19.906	19.802	55.810	40.330	5.307	15.298	0.2612	85.245
Candidate B	4.873	14.201	19.861	19.793	58.938	42.603	5.356	15.756	0.2268	85.421
Candidate C	4.644	14.464	19.927	19.871	54.267	41.128	5.271	14.231	0.1636	86.531

Table 6.2: MOGA optimal candidates

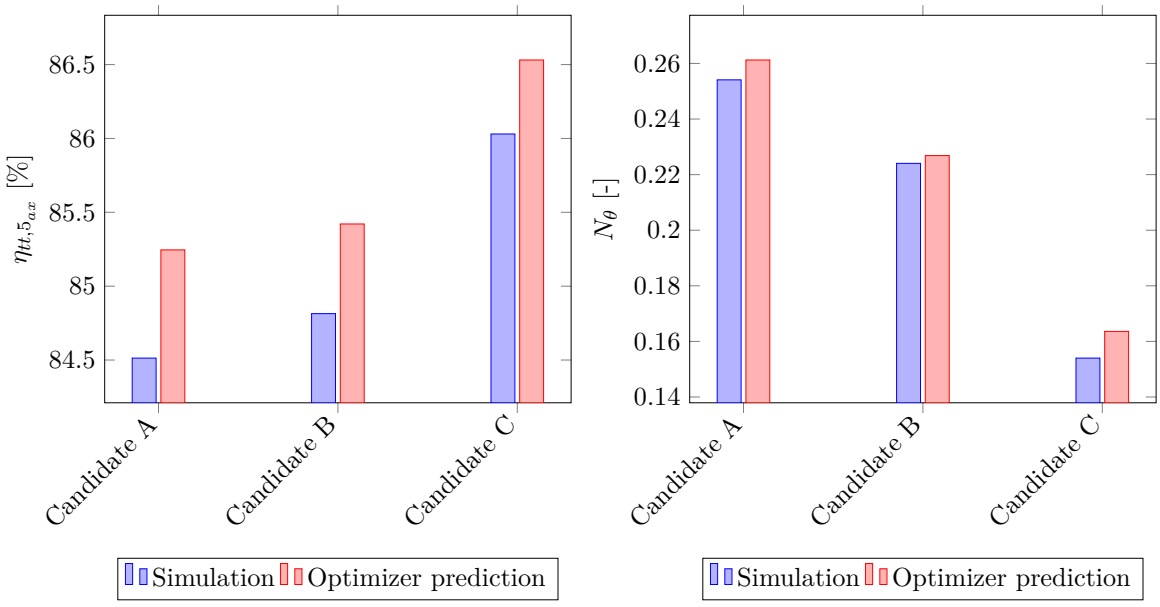

(a) Efficiency **(b)** Swirl coefficient

Figure 6.2: Verification data for MOGA

6.3.2 NLPQL candidates

The optimizer run with the non-linear programming by quadratic lagrangian was set up with the same criteria for optimizing rotor efficiency as mentioned in the previous section. The algorithm presents only one candidate point as compared to the three presented by MOGA. The candidate point was verified to the check the optimizers accuracy and was found to be within the expected bounds. The optimal candidate from the NLPQL optimization is represented in Table 6.3. The verification data for the efficiency and the swirl factor is shown in Figure 6.3a and 6.3b respectively. Unlike the case for MOGA where the optimizer over-predicts the values , for the NLPQL it under-predicts and this trend can be observed in Figure 6.3. Since the variation of the performance parameters is within allowable limits ($< 1\,\%$), the optimizer accuracy is sufficient to perform further analysis.

	$R_{hub,te}$ $[mm]$	$R_{shourd,te}$ $[mm]$	$R_{hub.le}$ $[mm]$	$R_{shourd,le}$ $[mm]$	β_{hub} [deg]	β_{shroud} [deg]	b_{le} $[mm]$	Z_{axial} $[mm]$	N_θ [-]	$\eta_{tt,5_{ax}}$ [%]
Objectives										Maximize
Baseline configuration	4.830	14.750	17.11	16.95	60	60.18	5.53	14.68	0.5056	78.13
Optimal design points										
Candidate D	4.610	14.295	20	19.932	58.891	40.00	5.48	15.361	0.2202	85.746

Table 6.3: NLPQL optimal candidate

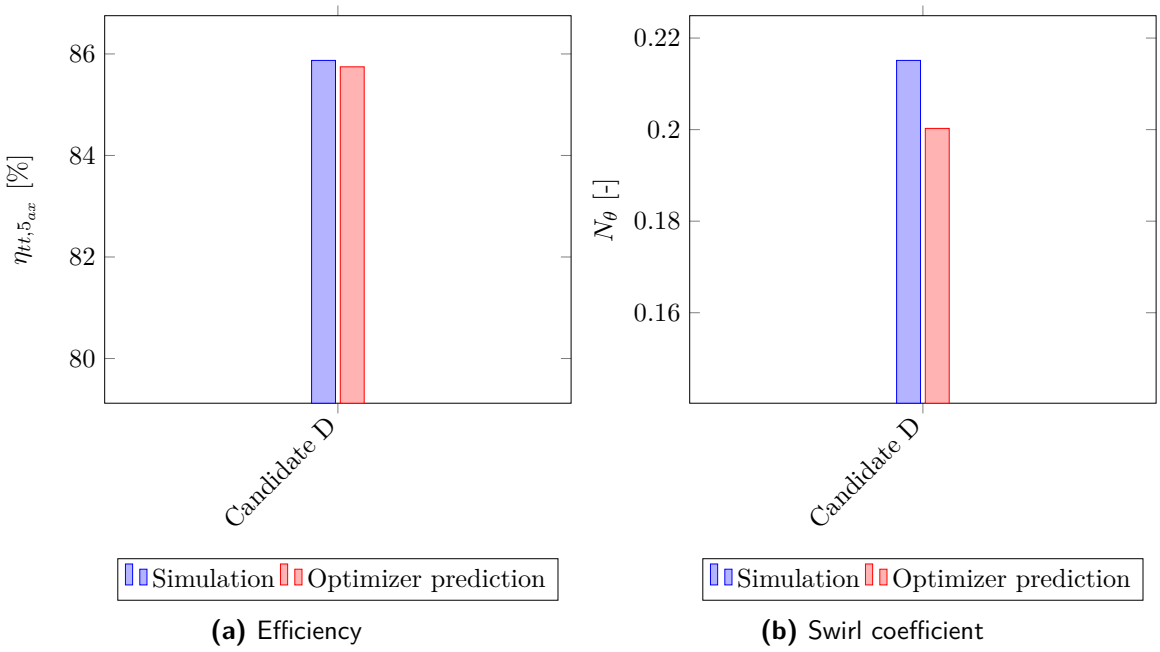

(a) Efficiency **(b)** Swirl coefficient

Figure 6.3: Verification data fro NLPQL

6.4 Performance analysis of the optimal candidates

The optimal candidates presented by the MOGA in Table 6.2 exhibit an increase in efficiency of a minimum of 7 percentage points and a maximum of 8.4 percentage points from the baseline design and the NLPQL algorithm shows an increase of 7.6 percentage points. In both cases, the trailing edge diameters do not change significantly and combined with the sensitivity analysis of efficiency in Section 6.2, it can be concluded that the major impact comes from the variation in tip diameters and the exducer angles. The variation in axial length also affects the efficiency due to a change in mass flow that occurs as a result. The tip width variation between the baseline and the optimized design in all cases is very minor and the change in other design parameters is considered to take into account any change in efficiency that occurs as a result.

All of the optimal candidates exhibit an increase of tip diameter. On average there is an increase of tip diameter by 16.6 %. Figure 6.4 shows the variation of efficiency with tip radii and it can be observed that with increase in the average tip radii, the efficiency increases. An increase in the tip radii leads to higher tip speeds and consequently a higher velocity

ratio than the baseline which translates to a higher efficiency The optimized rotors exhibit a velocity ratio of 0.7 and the baseline with a ratio of 0.58 and this can be seen in Figure 6.5. This is in accordance with the findings in literature [18].

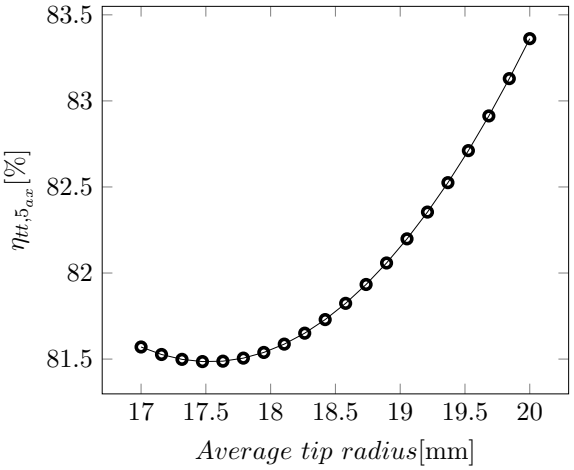

Figure 6.4: Efficiency as function of tip radii

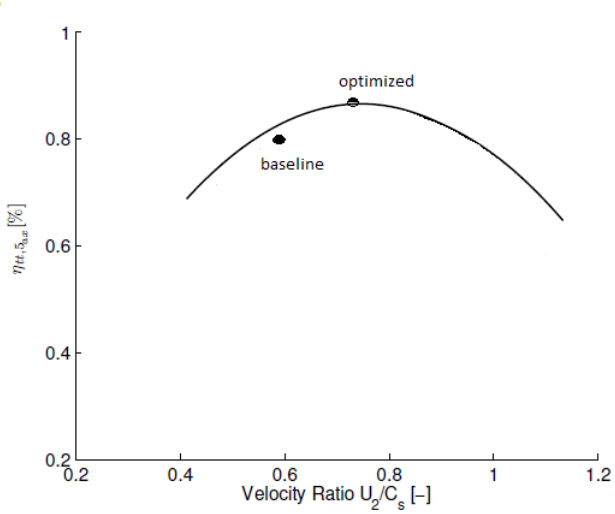

Figure 6.5: Efficiency as a function of velocity ratio

The efficiency equation defined in Chapter 3 is a function of the swirl energy. This energy lost due to the tangential component of velocity can be correlated with the swirl factor. In Figure 6.6a, the swirl energy is presented as a function of the swirl factor and this energy increases with increase in swirl factor. The baseline with a high swirl factor of 0.5056 exhibits the most swirl energy of 25 200 J/Kg and candidate C exhibits the least swirl factor of 0.1540 (value from CFX simulation) and a swirl energy of 2290 J/Kg. A reduction of the swirl leads to an improvement of efficiency and the trend can be visualized as in Figure 6.6b. This reduction of swirl factor between the baseline and the optimized design is achieved through a variation of the exducer angle.

From the sensitivity data in Figure 6.1, the high impact of the exducer angle on swirl reduction is made apparent. The exducer angle at shroud station has the greatest impact followed by the exducer angle at the hub station. The exducer angle at the hub station has a negative impact on efficiency and the optimized candidates are in the range of 55° to 60°. Only β_{shroud} has a positive impact and is consequently reduced to approximately 40° in almost all of the optimized candidate points. The parametric trends of the exducer shroud angle with the swirl and the efficiency are extracted using the baseline characteristics for the other design parameters at the response point. There is a significant reduction of swirl by almost 15 percentage points for a reduction in β_{shroud} from 60° to 40° as seen in Figure 6.7a. This is accompanied by a improvement in efficiency of 4.5 percentage points, see Figure 6.7b.

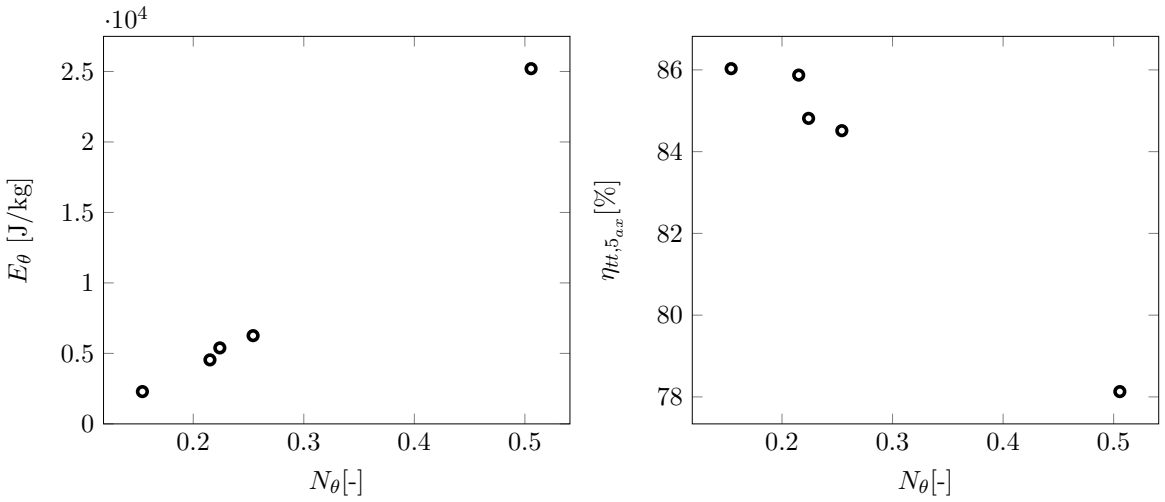

(a) Swirl energy **(b)** Efficiency

Figure 6.6: Performance analysis of optimized candidates with respect to swirl factor

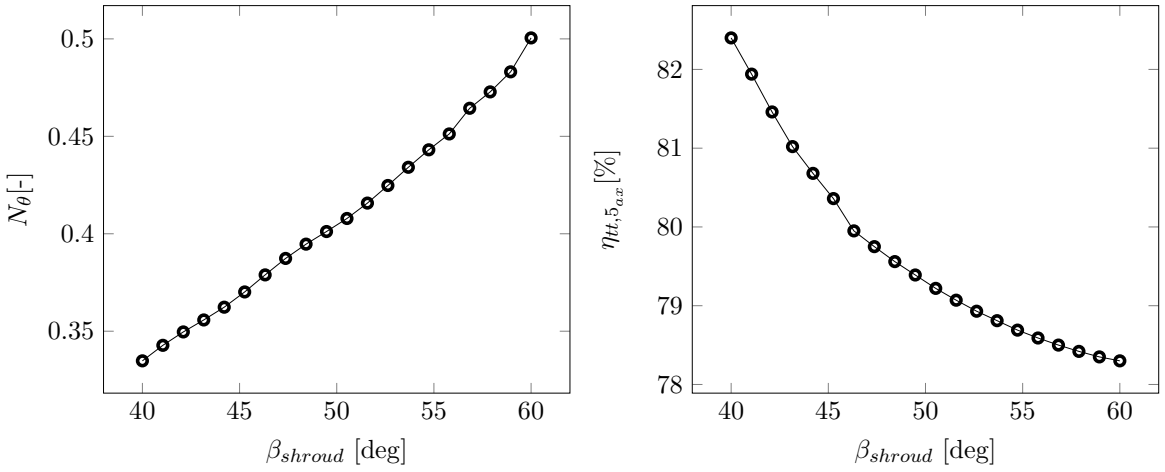

(a) Swirl factor **(b)** Efficiency

Figure 6.7: Performance analysis of optimized candidates with respect to exducer angle

One the side-effects of this modification in geometry is the change in mass flow rate through the system. The increase in mass flow rate can be attributed to the increase in passage area.

This might cause a mismatch with other components of the MTT power unit which could be overcome by redesigning the volute. However, this is beyond the scope of the current thesis. This mass flow mismatch is considered as a limitation of the thesis work. Figure 6.8 shows a comparison of mass flow rate between the optimized candidates and the baseline.

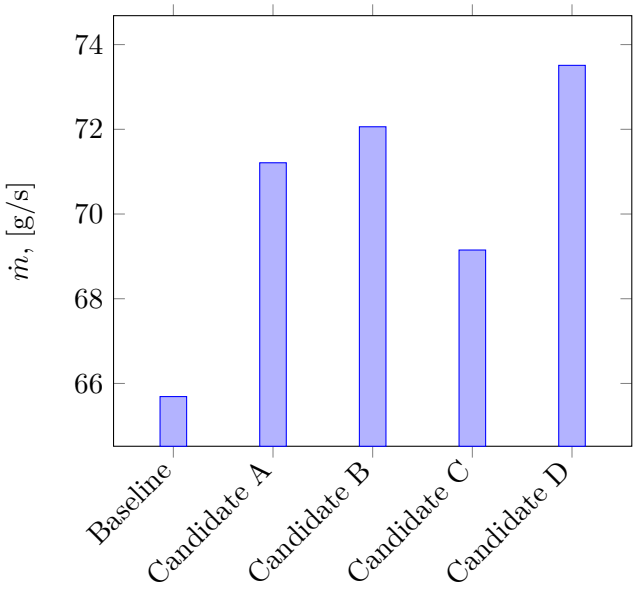

Figure 6.8: Mass flow rate variation

6.5 Design study of the optimal candidates with diffuser

For the baseline rotor and optimal candidates mentioned in Section 6.3, simulations are performed including the diffuser domain to study the interactions between them and account for the variation in diffuser performance. The total-to-static efficiency definition($\eta_{ts,9}$) is used to evaluate the overall performance since at the diffuser exit, the dynamic head is of a small magnitude and can be neglected. The coefficient of pressure (C_p) is used to quantify the diffuser performance. A total inlet pressure of 2.82 bar, total inlet temperature of 1285 K, a static outlet pressure at diffuser exit is atmospheric pressure and a rotational speed of 240 000 rpm for the rotor is specified as the boundary conditions. The walls are modelled as adiabatic, smooth, no slip walls. A mixing plane which averages the quantities across the surface is used for modelling the rotor-diffuser interface. The rotor and diffuser performance characteristics are shown in Table 6.4.

With reduction in rotor exit swirl, it can be observed that the diffuser performance is improved. However, this improvement in C_p is only until a certain swirl after which the performance drops again. This phenomena is better explained by visualizing the flow field as shown in Figure 6.9. At high swirls, there is more recirculation as shown in Figure 6.9a and this leads to a drop in diffuser performance. With decrease in swirl, this recirculation zone reduces in size, see Figure 6.9b. If the swirl coefficient is reduced beyond a critical value, it

would lead to lower velocities close to the wall and boundary layer separation would occur which will result in a performance drop, see Figure 6.9c . The optimal candidate D exhibits a smaller recirculation zone than the baseline (N_θ=0.4764) and candidate C (N_θ=0.1619) and consequently has a 17.66 percentage point improvement in pressure recovery. From Table 6.4 and diffuser flow field visualization for the baseline and the optimized candidates, it is apparent that the optimum swirl coefficient is approximately 0.22. One of the drawbacks of this unsteady characteristic due to the high adverse pressure gradients is that there are issues with the convergence of the solution. The rotor and diffuser performance parameters showed oscillations at convergence. The performance characteristics are reported in table 6.4 with error bars is shown in Figure 6.10. The fluctuations of the coefficient of pressure are more pronounced as compared to that of the total-to-static efficiency and this is expected given the higher degree of pressure variation in the diffusive segment of the fluid domain.

One of the important observations is that the rotor efficiency when coupled with the diffuser is lesser as compared to the optimization simulations done with the rotor domain alone. This can be explained based on the additional pressure losses generated when coupled with the diffuser domain, see Figure 6.11. In Table 6.4, the results from the study are tabulated. It is important to note that the power represented in the table below is the shaft power. An average of 7 to 8 percentage point improvement in rotor efficiency compared to the baseline is observed. However, the improvement in total-to-static efficiency when coupled with the diffuser domain is less than half of that. There is a minimum of 1.1 percentage point improvement as exhibited by candidate A and a maximum of 3.22 percentage point improvement shown by candidate C. The maximum diffuser performance obtained is 49.12 % (candidate D). An increase in the diffuser performance would lead to a decrease in static pressure at diffuser inlet which in turn would increase the diffuser inlet velocities and additional pressure losses would incur in the system. Consequently a lesser magnitude of improvement in total-to-static efficiency is seen as compared to the rotor efficiency and it is clear that the design of the diffuser is a very delicate matter.

The design solution with the highest total-to-static efficiency of 66.72 % and the highest rotor efficiency of 83.39 % (candidate C) is not the one with the best diffuser performance. As explained earlier, the rotor performs better with a lower swirl factor but for the diffuser decreasing the swirl factor beyond a point($\sim<22\%$) leads to a drop in performance. Candidate D has the optimum swirl factor for diffuser performance but has a lesser total-to-static and lesser rotor efficiency as compared to candidate C. In other words there is compromise between rotor and diffuser performance. From these analysis it is clear that 'Candidate C' has the best overall performance characteristics.

	$\dot{m}$ $[g/s]$	C_p [%]	N_θ [-]	$\eta_{tt,5_{ax}}$ [%]	$\eta_{ts,9}$ [%]	P $[kW]$
Baseline	65.81	31.461	0.4764	74.85	63.49	13.99
Candidate A	71.85	47.67	0.2413	81.01	64.59	15.21
Candidate B	68.77	45.17	0.2015	81.99	65.17	15.54
Candidate C	73.17	44.16	0.1619	83.39	66.72	15.81
Candidate D	70.82	49.12	0.2206	82.78	66.14	15.68

Table 6.4: Design study with diffuser

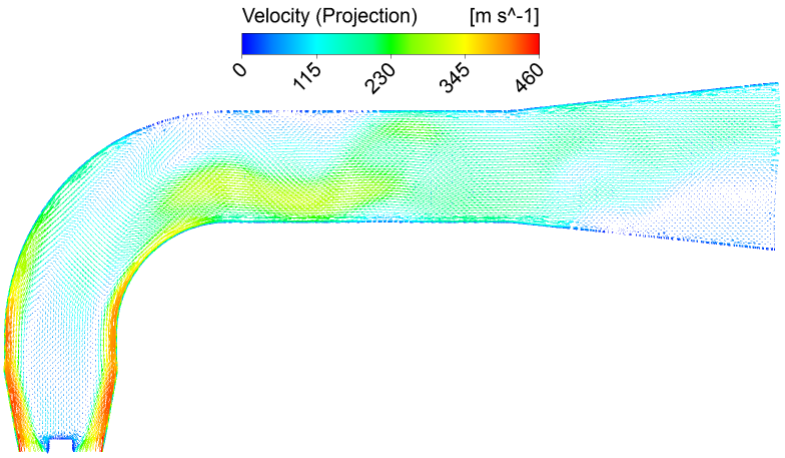

(a) Diffuser with baseline rotor (N_θ =0.47)

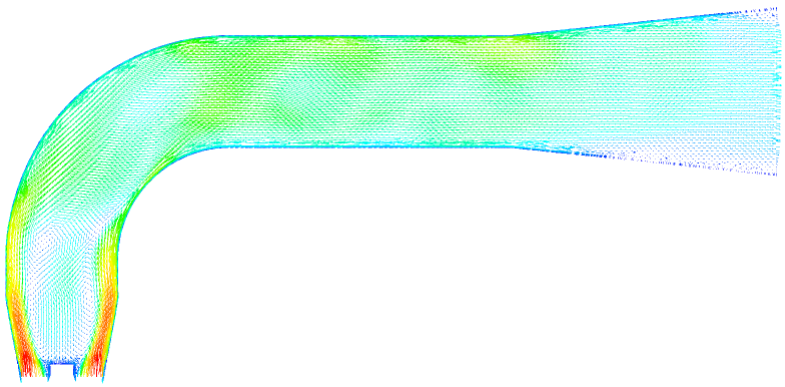

(b) Diffuser with candidate D (N_θ =0.22)

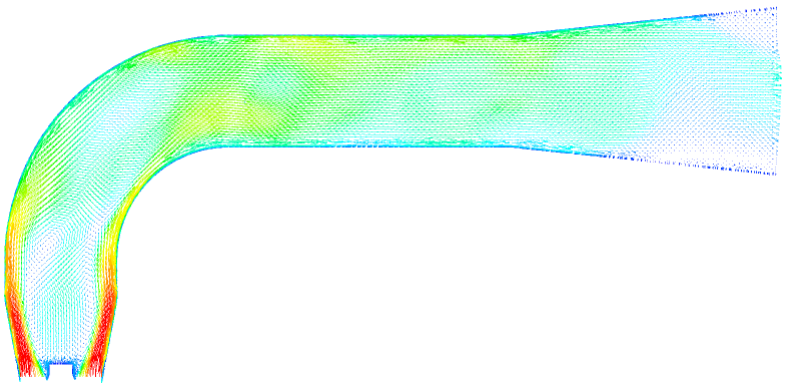

(c) Diffuser with candidate C (N_θ =0.16)

Figure 6.9: Diffuser flow field visualization

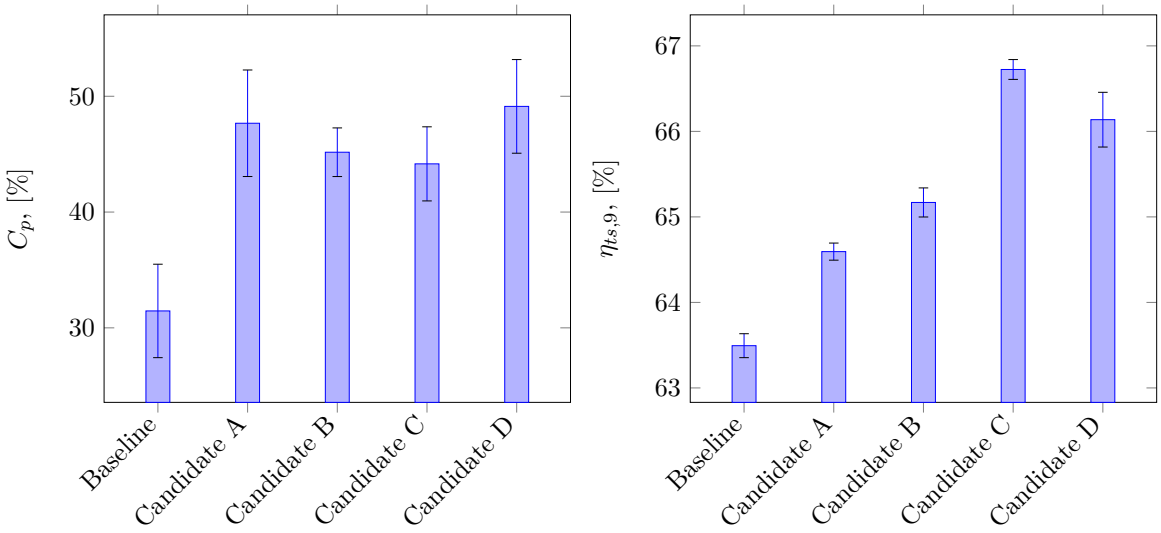

(a) Coefficient of pressure recovery **(b)** Total-to-static efficiency

Figure 6.10: Performance parameters with error bars representing fluctuations

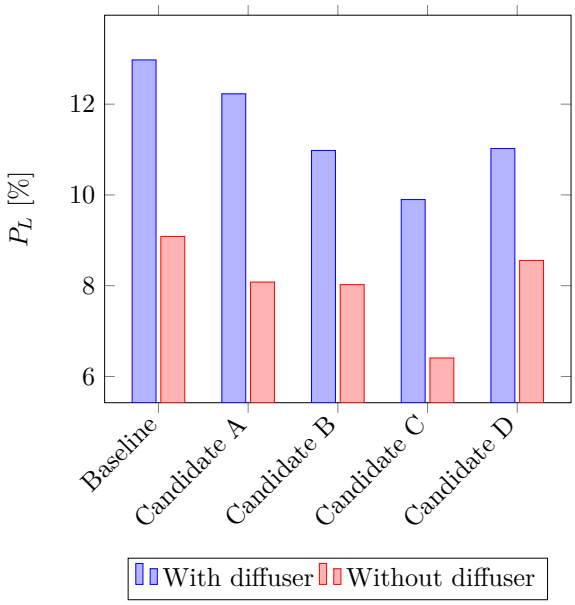

Figure 6.11: Relative pressure loss for simulations with and without diffuser domains

6.6 Fluid dynamic analysis of the optimal turbine configuration

The rotor geometry consists of 9 blades and is axis-symmetric and consequently for the fluid flow analysis only a 40° sector model is used. The completer rotor geometry for both the baseline and the optimized solution in top view is represented in Figure 6.12.

The velocity triangles at inlet and outlet at rotor midspan can be visualized in Figure 6.13. The optimized rotor has a larger tip diameter and lesser tip width. Consequently it exhibits a higher tip speed and the relative inflow angle becomes negative .The baseline has lesser tip speeds due to the lower tip diameter and exhibits a positive relative inflow angle ,see Figure 6.13a. From the 0-D model in [3], negative relative inflow angles reduces the incidence losses and consequently the optimal candidate benefits from such a change in flow direction. At the outlet, it is clear that the tangential component is reduced in the optimized geometry and this can be attributed to the lower exducer angles at the trailing edge. This reduction in the tangential component at rotor exit reduces the swirl energy loss and enhances the efficiency. Consequently it shows a total-to-total ($\eta_{tt,5_{ax}}$) improvement of 8.533 percentage points and a total-to-static efficiency enhancement of 3.229 percentage points.

The baseline exhibits a higher degree of adverse pressure gradients between the blade passage as compared to the optimized rotor. These adverse pressure gradients and high speeds make the baseline configuration more susceptible to shock induced separations especially at the trailing edge. From Figure 6.14, it can be observed that the trailing edge for the baseline exhibits higher velocities and consequently exhibits a stronger shock wave. This characteristic will also affect the performance of the diffuser downstream of the rotor. Moreover from the point of aerodynamic loading on the blade, the optimized rotor experiences lesser forces as compared to the baseline configuration, see Figure 6.15. However, note that the higher tip diameter of the optimized rotor will lead to higher centrifugal loading, this will be discussed in greater detail in the next chapter.

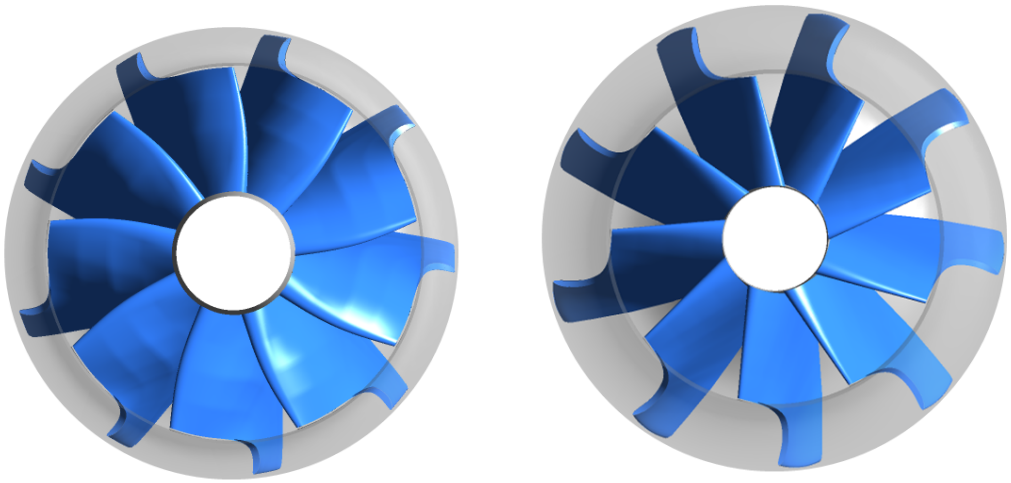

(a) Baseline rotor geometry **(b)** Optimized rotor geometry

Figure 6.12: Rotor geometry top view

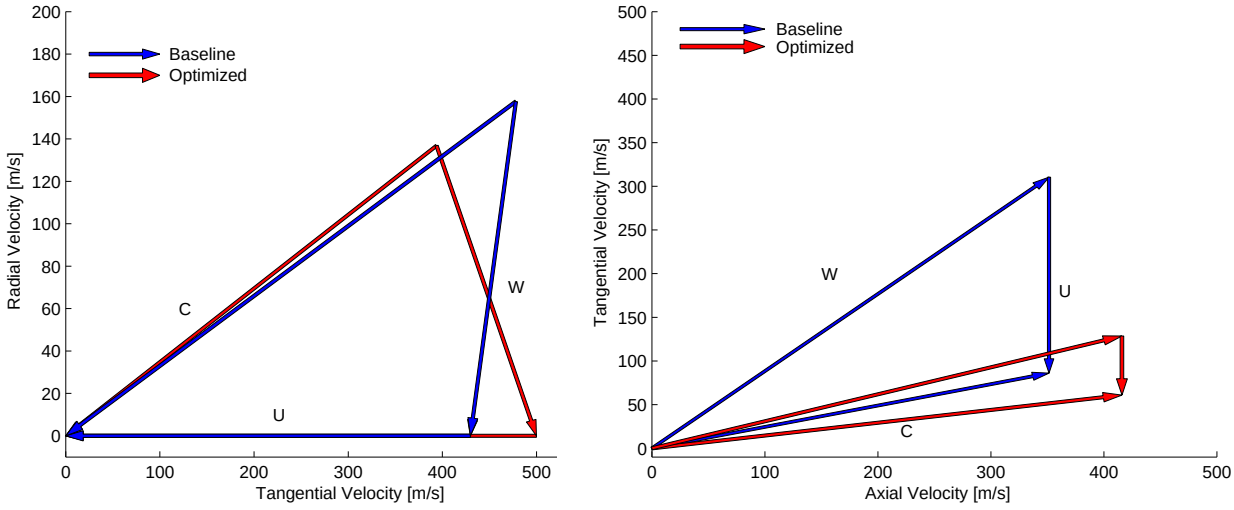

(a) Rotor inlet **(b)** Rotor outlet

Figure 6.13: Velocity triangles for the baseline and optimized geometry

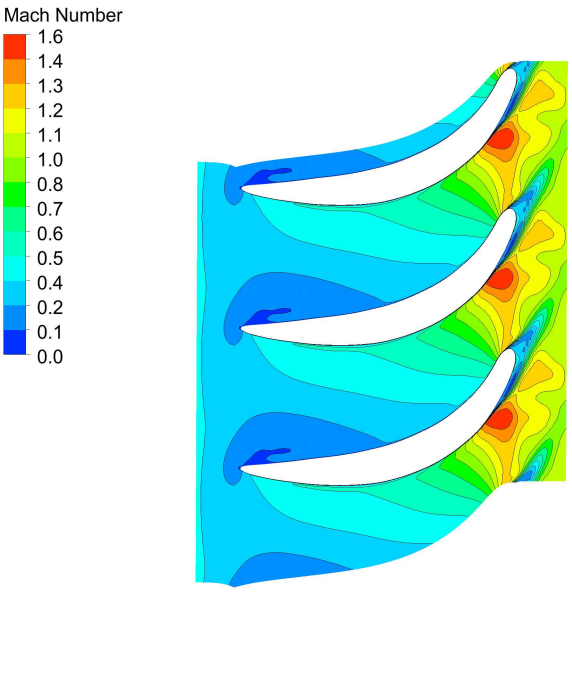

(a) Baseline rotor relative Mach number contour

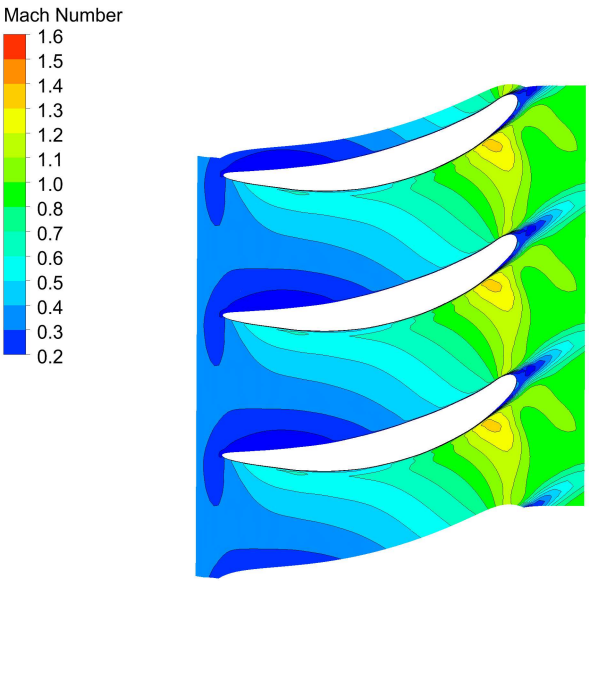

(b) Optimized rotor relative Mach number contour

Figure 6.14: Relative Mach number contours in blade-to-blade view at midspan

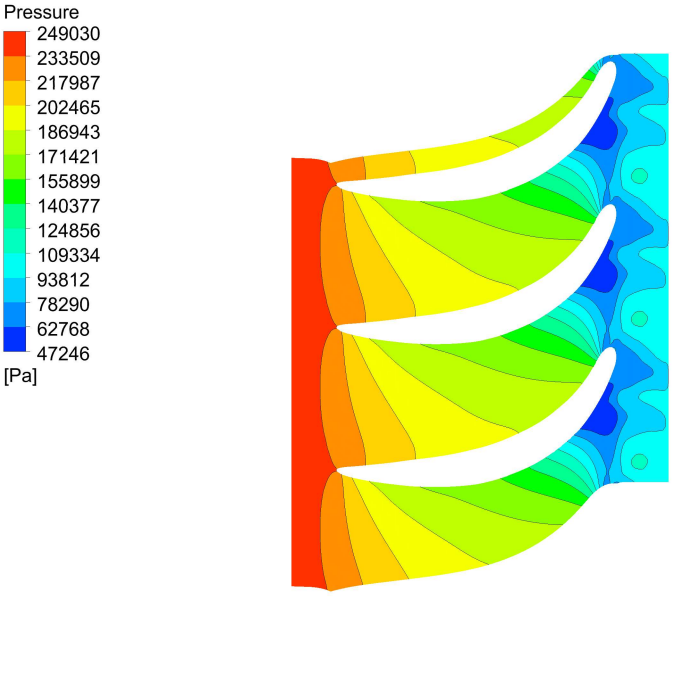

(a) Baseline rotor pressure contour

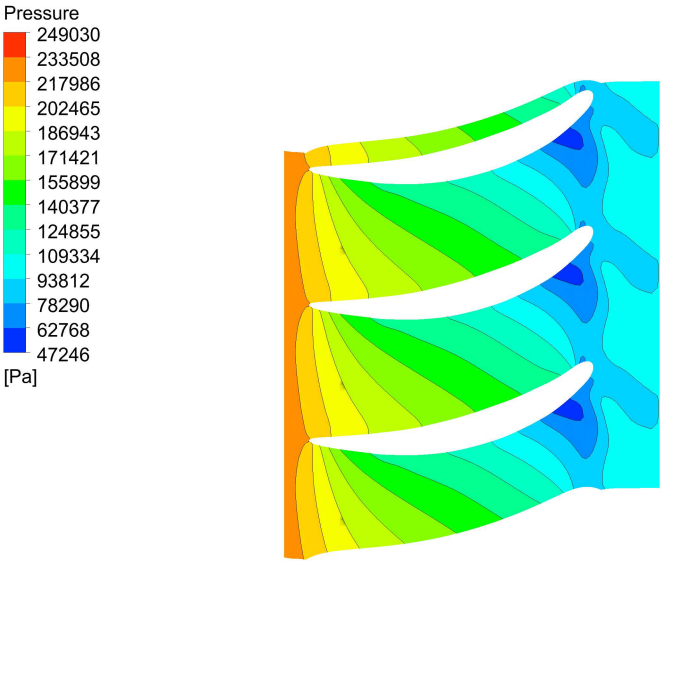

(b) Optimized rotor pressure contour

Figure 6.15: Pressure contours in blade-to-blade view at midspan

Chapter 7

Stress Analysis of the Optimal Turbine Configuration

7.1 Mechanical analysis

In the previous chapter, an aerodynamic optimization is performed and the performance improvements have been analysed. As mentioned, the modifications on the rotor geometry have a direct consequence on mechanical stresses. ANSYS mechanical is used for performing the stress analysis on the rotor geometry. The mesh and solver settings used for the stress analysis are mentioned in Chapter 4. The material used for the stress modelling is INCONEL 713C whose properties are specified in Table 4.4. The rotor geometry is modelled as a 40° sector with a shaft and a comparison is made between the von-Mises stresses of the baseline geometry and the optimal solution.

7.1.1 Comparison at max speed

In this section, a stress analysis is carried out at a speed of 240 000 rpm and aerodynamic loads, i.e. surface pressure distribution are imported from the fluid flow simulations done in the previous chapter. Stress probes are inserted at different stations to gain insight on the stress levels at different stations. The equivalent Von-mises stresses for the baseline and optimal candidate are compared. In both the cases, higher stresses occur close to the hub section of the rotor. This is expected since the weight of the entire blade is supported in the hub section. The optimized rotor has a larger tip diameter as compared to the baseline and experiences larger centrifugal loads which directly translates to higher tip stresses as compared to the baseline. The baseline stress contours with stress probes are represented in 7.1. The optimized rotor also has a lower exducer angle , reduced axial length and hence it

experiences a reduction in stress levels at the trailing edge station which is apparent from the stress probes in Figure 7.2. The maximum values of stresses for the baseline occur at the trailing edge section near the root, see Figure 7.3. Conversely, for the optimized rotor it is closer to the shaft, see Figure 7.4.

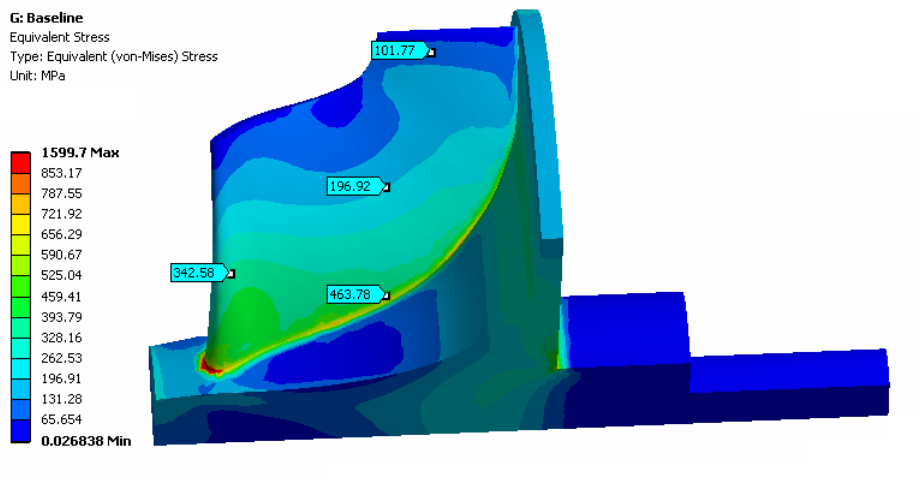

Figure 7.1: Baseline stress

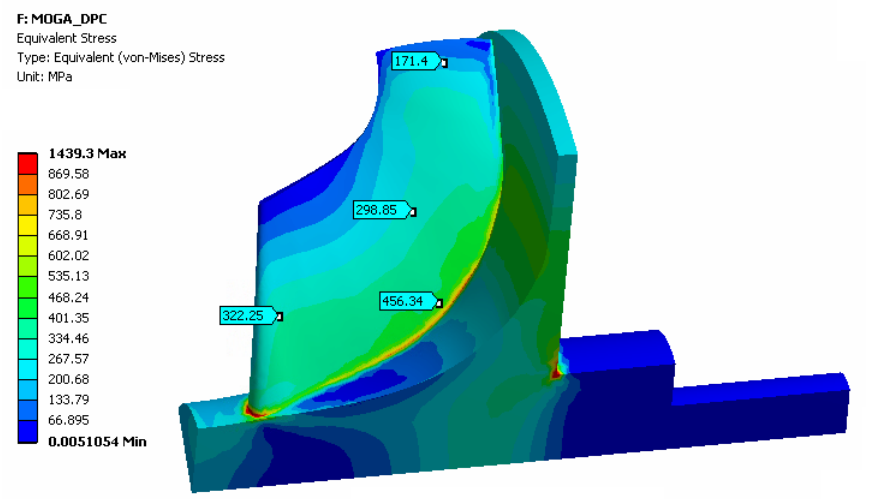

Figure 7.2: Optimized rotor stress

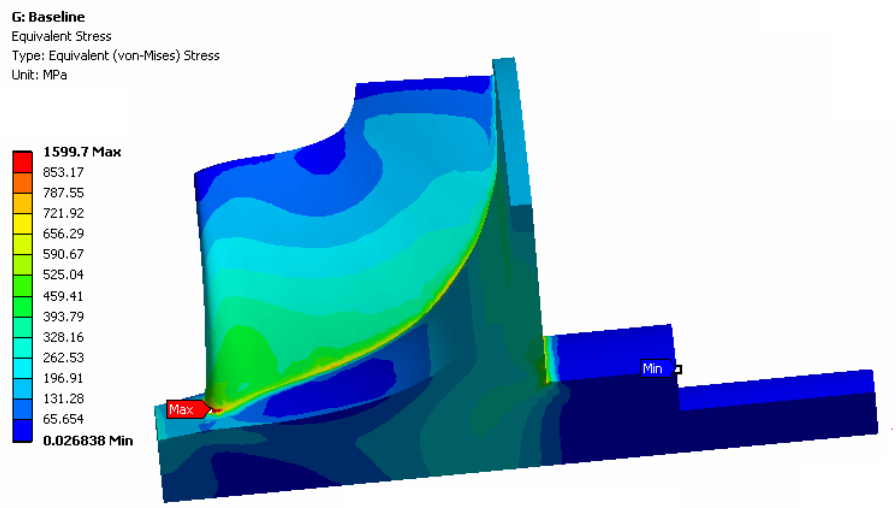

Figure 7.3: Baseline stress

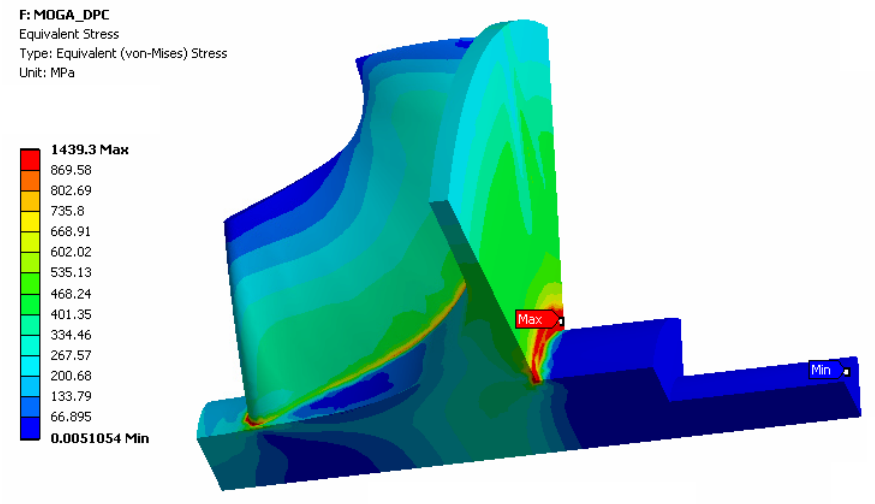

Figure 7.4: Optimized rotor stress

7.1.2 Analysis with varying speeds of rotation

The optimized rotor exhibits higher stress levels close to the tip. For the application at hand with high temperatures especially at the tip increased stress levels may reduce the turbine life and also lead to a reduction of the creep life. Consequently a reduction in speed to reduce the tip stress levels back to baseline levels would be beneficial. Before performing the finite element analysis, a simple calculation is performed to get an overview of the approximate speed reduction that needs to be incorporated to reduce the stress levels to that of the baseline geometry at the tip station. The centrifugal loading is more predominant than the aerodynamic loads especially at higher speeds and consequently the calculation takes into account only the centrifugal loading. The centrifugal force is defined according to Eq 7.1 and stress are directly proportional to the force. Although the change in area between the two geometries and aerodynamic loads must also be taken into account , for the preliminary analysis these effects are discarded and only the effect centrifugal loading is considered.

The baseline stress at tip station is 101.82 MPa and for the rotor geometry it is 171.74 MPa. Using Eq. 7.1, the new speed of rotation required to achieve the reduction in stress levels is approximately 185 000 rpm. Consequently the simulations are performed for the speeds ranging from 240 000 rpm to 240 000 rpm to 180 000 rpm and the results from this analysis are represented in Table 7.1. As expected with reduction in speeds, the stress levels reduce drastically especially the maximum values and those at the tip station. The approximation in 7.1 more or less predicts the range in which the speed reduction needs to be achieved and it is clear from table 7.1 that a speed reduction to around 180 000 rpm is required to achieve baseline stress levels at the tip station. Figure 7.5 shows the stress contours at 180 000 rpm with probes at the tip station and the maximum and minimum stress nodes.

It is important to note that the aerodynamic optimization in the previous chapter is performed at 240 000 rpm and if the speed is reduced, this is no longer the optimal rotor geometry. The above analysis is conducted with varying speeds of rotation in order to provide an indication of how the speed impacts the stress levels for the optimized design and to provide data for future decisions of MTT.

$$F = mR\omega^2 \ , where \ \omega = \frac{2\pi N}{60} \tag{7.1}$$

Rotor geometry specification	N [rpm]	Von-Mises stress [MPa]		
		Tip Station	Maximum	Minimum
Baseline	240000	101.82	1599.7	0.02684
Optimized	240000	171.74	1439.3	0.00510
Optimized	220000	144.63	1209.4	0.00429
Optimized	200000	119.98	999.5	0.00354
Optimized	190000	108.59	902.1	0.00320
Optimized	180000	97.767	809.5	0.00287

Table 7.1: Structural analysis with varying speeds of rotation

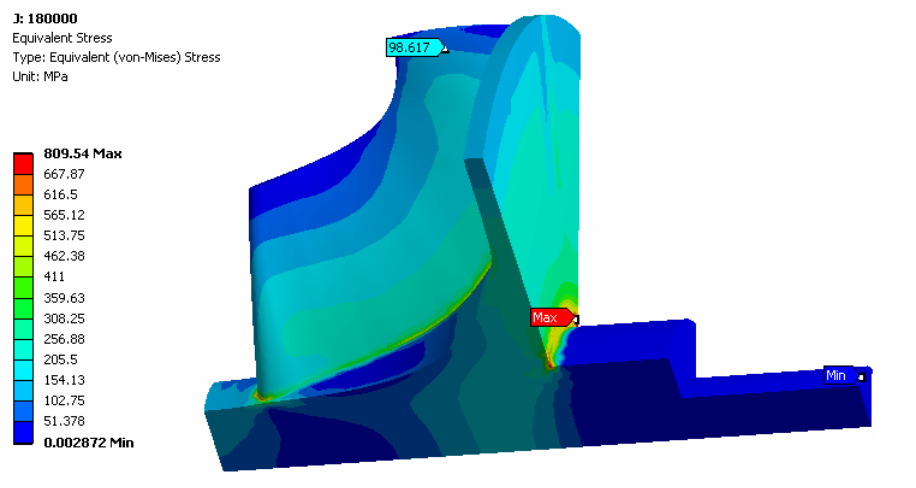

Figure 7.5: Optimized rotor stress contours at $180\,000\,\mathrm{rpm}$

Chapter 8

Conclusions and Recommendations

This work illustrated the optimization of the MTT micro turbine design using a 3-D CFD model. The rotor geometry was parametrized using the tip radii(the hub and shroud radii at leading edge), the hub and shroud radii at trailing edge and exducer angles. A goal driven optimization was initially performed to optimize the rotor geometry with the objective of improving the total-to-total efficiency ($\eta_{tt,5_{ax}}$) using the NLPQL and MOGA algorithms. The important conclusions from this optimization were as follows:

- From the parametric sensitivity it was clear that all of the six design variables have a significant impact on efficiency. The exducer angles have the most predominant effect on efficiency with that of β_{shroud} larger than β_{hub}.
- The best candidate from the MOGA algorithm exhibited an increase of rotor efficiency of 7.90 percentage points (Candidate C) and the NLPQL candidate point with an improvement of 7.74 percentage points. This efficiency improvement was accompanied by an increase of mass flow rate with a minimum of 69.15 g/s (Candidate B) and a maximum of 73.51 g/s (Candidate C) as compared to the baseline value of 65.69 g/s.

The optimized candidates are analysed using simulations with the diffuser domain and the main findings from these studies were as follows:

- The total-to-total efficiency of the rotor drops by 3 percentage points on an average due to the additional pressure losses introduced when coupled with the diffuser.
- The diffuser performance has increased from 31.46 % at the baseline to a maximum of 49.13 % exhibited by Candidate D at a swirl coefficient of 0.22. If the swirl coefficient is increased or decreased from this optimum, diffuser performance drops. The best design solution in terms of efficiency is Candidate C with $\eta_{tt,5_{ax}}$=83.38 % and with $\eta_{ts,9}$=

66.72 %. Candidate C however exhibits a poorer diffuser performance with C_p=44.16 % at a swirl coefficient of 0.162. From this study, it is apparent that there is compromise between rotor and diffuser performance.

- The improvement in rotor efficiency($\eta_{tt,5_{ax}}$) has a maximum of 8.54 percentage points (Candidate C) as compared to the baseline which is more or less similar to the case with the individual rotor domain simulations. The improvement in total-to-static efficiency ($\eta_{ts,9}$) achieves only a maximum of 3.23 percentage points(Candidate C) as compared to the baseline. In other words ,whatever is gained in rotor total-to-total efficiency from the design optimization, less than half of it is utilized when coupled with the diffuser(C_p<50 %).

The best design solution (Candidate C) is analysed from a structural point of view and compared with the baseline design. The equivalent Von-mises stresses are compared and the most important outcomes from this analysis are as follows:

- The optimized rotor exhibits a stress of 171.74 MPa at the tip station ,whereas the baseline experiences a stress of 101.82 MPa. This can be attributed to the increase in tip diameter by a factor of 1.16 for the optimized configuration as compared to the baseline. At the root section both geometries exhibit higher stresses than most of the other stations. At the trailing edge the optimized rotor exhibits a stress of 322.25 MPa which is lesser than the baseline geometry with 342.58 MPa. A maximum stress of 1599.7 MPa for the baseline occur at the trailing edge root section and the optimized rotor experiences a lower maxima of 1439.3 MPa and it occurs closer to the shaft.
- In order to reduce the tip stresses for the optimized rotor and bring them closer to the baseline values, the speed of rotation must be reduced to the neighbourhood of 180 000 rpm.

The following are the recommendations from this thesis work:

- There is a compromise between diffuser and rotor performance, consequently a coupled optimization is recommended with the diffuser domain in order to get a better understanding of the interaction effects between the components. The optimization procedure in this work is performed with only the rotor domain due to computational restrictions and the design solution does not take into account the diffuser performance during the optimization process.
- A scaling study with the volute is recommended for the optimized rotor geometry in order to restrict the mass flow rate. The design solution exhibits an increase in passage area and consequently a rise in mass flow rate. However, in the real application a change in mass flow rate might cause a mismatch with other components of the MTT power unit.
- The structural analysis is done post optimization and is carried out without any constraints for maintaining the stress within acceptable levels. Therefore a multi-disciplinary optimization combining the solid and fluid analysis is recommended to prevent the stress increase and maintain the creep life of the component.

Bibliography

[1] Soares, C., 2011. *"Microturbines : Application for Distributed Energy Systems"*. Butterworth-Heinemann.

[2] Sol, W.K., 2012. *"Radial Micro Turbine Design Optimization"* Master Thesis, Delft University of Technology.

[3] Gideonse, K.W., 2014. *"Design Optmization of a Radial Micro Turbine"* Master Thesis, Delft University of Technology.

[4] Visser, W.P.J., Shakariyants, S.A., de Later, M.T.L., Haj Ayed, A., and Kusterer, K., 2012. *"Performance Optimization of a* 3 kW *Microturbine for CHP Applications"* Proceedings of ASME Turbo Expo GT2012, 68686.

[5] Saravanamuttoo, H.I.H.,Rogers, G.F.C. and Cohen,H., 2011. *"Gas Turbine Theory."*5th ed. Pearson Education.

[6] Visser, W.P.J., Shakariyants, S.A., and Oostveen, M., 2011. *"Development of a* 3 kW *Microturbine for CHP Applications"* Journal of Engineering for Gas Turbines and Power, 133, 042301-1.

[7] Peirs, J., 2008. *"Ultra micro gas turbine generator"* Katholieke Universiteit Leuven, Department of Mechanical Engineering.

[8] Waumans, T., Vleugels, P., Peirs, J., Al-Bender, F., Reynaerts, D., 2006. *"Rotordynamic behaviour of a micro-turbine rotor on air bearings: modelling techniques and experimental veriiňĄcation, p. 182"* ISMA. International Conference on Noise and Vibration Engineering.

[9] van Buijtenen, J.P., and Visser, W.P.J., 2007. *"Gas Turbines WB4420"* Delft University of Technology.

[10] Earl Logan, Jr.,Roy, R., 2003. *"Handbook of Turbomachinery"* 2nd ed. ,MARCEL DEKKER INC.

[11] Çengel, Yunus A., and Boles, M.A., 2011 . *"Thermodynamics An Engineering Approach"* 7^{th} edition. New York: McGraw-Hill.

[12] Eijgelshoven, T., 2011 *"Initial turbine component optimization study for the MTT micro turbine"* Master Thesis, Delft University of Technology.

[13] Aungier, R. H., 2006. *"Turbine Aerodynamics : Axial-Flow and Radial-Inflow Turbine Design and Analysis"*. ASME press.

[14] Simpson, A.T., Spence, S.W.T., and Early, J.K., 2009. *"A numerical and experimental study of the rotor inlet flow fields of radial turbines using vaned and vaneless stators"* ASME Turbo Expo 2009: Power for Land, Sea, and Air (pp. 1385-1395).

[15] Abidat, M., Hamidou, M.K., Hachemi, M., and Hamel, M., 2006. *"Design and Flow Analysis of Radial and Mixed Flow Turbine Volutes* European Conference on Computation Fluid Dynamics, ECCOMAS CFD.

[16] Japikse, D., and Baines, N.C., 1994. *"Introduction to turbomachinery"* Concepts ETI Oxford University Press.

[17] Deng, Q., Niu, J., Mao, J., and Feng, Z. (2007, January). *"Experimental and Numerical Investigation on Overall Performance of a Radial Inflow Turbine for* 100 kW *Mircoturbine"*In ASME Turbo Expo 2007: Power for Land, Sea, and Air (pp. 919-926). American Society of Mechanical Engineers.

[18] Dixon, S. L., and Hall, C., 2013. *" Fluid mechanics and thermodynamics of turbomachinery"*. Butterworth-Heinemann.

[19] Ford, H., & Alexander, J. M., 1963. *"Advanced mechanics of materials"*(p.455)London: Longmans.

[20] Whitfield, A., and Baines, N.C., 1990. *"Design of Radial Turbomachines"* Longman Scientific and Technical.

[21] Mueller, L., Alsalihi, Z., and Verstraete, T., 2013. *"Multidisciplinary optimization of a turbocharger radial turbine"* Journal of Turbomachinery, 135(2), 021022.

[22] Wilcox, D.C., 2006. *"Turbulence Modeling for CFD"* 3rd ed., DCW Industries.

[23] Spalart, P. R., 2000. *" Strategies for turbulence modelling and simulations"* International Journal of Heat and Fluid Flow, 21(3), 252-263.

[24] Rahbar, K., Mahmoud, S., Al-Dadah, R. K., and Elsayed, A., 2013. *"Modeling and CFD Analysis of a Miniature Radial Turbine for Distributed Generation Systems"* International Conference of Applied Energy.

[25] Bradshaw, P., 1972. *"The understanding and prediction of turbulent flow"* Aeronaut. J, 76(739), 403-418.

[26] Menter, F. R., 1994. *"Two-equation eddy-viscosity turbulence models for engineering applications"* AIAA journal, 32(8), 1598-1605.

[27] Sarkar, A., and So, R. M. C., 1997. *" A critical evaluation of near-wall two-equation models against direct numerical simulation data"* International Journal of Heat and Fluid Flow, 18(2), 197-208.

[28] Davis, J. R. (Ed.)., 1997. *" ASM specialty handbook: heat-resistant materials"*. Asm International.

[29] Montgomery, D. C., 1984. *"Design and analysis of experiments"*. Vol. 7. New York: Wiley.

[30] Simpson, T. W., Poplinski, J. D., Koch, P. N., and Allen, J. K., 2001. *"Metamodels for computer-based engineering design: survey and recommendations"* Engineering with computers, 17(2), 129-150.

[31] Antony, J., 2014. *" Design of experiments for engineers and scientists"*. Elsevier.

[32] Giri, N. C., 1986. *"Design and analysis of experiments"*. New Age International.

[33] Hardle, W., 1990. *"Applied nonparametric regression"*. Vol. 27. Cambridge: Cambridge university press.

[34] Stein, M. L., 2012. *"Interpolation of spatial data: some theory for kriging"*. Springer Science and Business Media.

[35] Nocedal, J., and Wright, S., 2006. *"Numerical optimization"*. Springer Science and Business Media.

[36] Fonseca, C. M., and Fleming, P. J., 1995. *"An overview of evolutionary algorithms in multiobjective optimization"*. Evolutionary computation, 3(1), 1-16.

[37] Deb, K., Pratap, A., Agarwal, S., and Meyarivan, T. A. M. T., 2002. *"A fast and elitist multiobjective genetic algorithm: NSGA-II. Evolutionary Computation"*. IEEE Transactions, 6(2), 182-197.